# Assessment of the urban climate model MUKLIMO_3 for three heat waves in Bern

Master Thesis
Faculty of Science, University of Bern

handed in by
**André Hürzeler**

**2021**

Supervisor
**Prof. Dr. Stefan Brönnimann**

Advisors
**Dr. Moritz Gubler**
**Moritz Burger**

# Content

**Keywords:** urban climate modelling, urban heat island, MUKLIMO_3, urban temperature measurements

# Title:

# Assessment of the urban climate model MUKLIMO_3 for three heat waves in Bern

## Authors:

André Hürzeler[1,2], Moritz Burger[1,2], Moritz Gubler[1,2,3] & Stefan Brönnimann[1,2]

## Affiliation:

[1]Oeschger Center for Climate Change Research, University of Bern, Bern, 3012, Switzerland

[2]Institute of Geography, University of Bern, Bern, 3012, Switzerland

[3]Institute for Lower Secondary Education, Bern University of Teacher Education, 3012, Switzerland

## *Corresponding author:

André Hürzeler (andre.huerzeler@students.unibe.ch)

# Abstract

Extreme heat waves are a health hazard that will increase in the future, and which particularly affects urban populations worldwide due to intensification by urban heat islands. This study examined the performance of the urban climate model MUKLIMO_3 of the German Weather Service in modelling spatial air temperature patterns in the greater urban area of Bern, Switzerland, with a horizontal resolution of 50 to 200 m during three distinct heat waves in 2018 and 2019 over a total of 23 days. The validation of MUKLIMO_3 using low-cost air temperature data from more than 70 measurement locations showed that the air temperature distributions were modelled realistically. During daytime, air temperatures in MUKLIMO_3 were lower across all validation locations compared to the measured values with maximum median air temperature biases of -3.7 K to -4.8 K in the late afternoon. At night, MUKLIMO_3 showed a slowed cooling, so that higher air temperatures occurred in the first half of the night compared to the measured values with median air temperature biases of 1.5 K to 2.8 K at midnight. During the second half of the night, the median air temperature biases were reduced, so that the minimum air temperature in the morning was modelled very accurately with a median air temperature bias of 0.2 K to 0.7 K. Further, periods with increased mesoscale weather influences, such as cold air advections, likely lead to greater uncertainties in MUKLIMO_3 due to the absence of their implementation in the model.

# 1. Introduction

Changes in numerous extreme weather events have been observed globally since the mid-20th century, such as an increase and intensification of daily temperature extremes. Anthropogenic heating has more than doubled the likelihood of heat waves in many regions, leading to increased heat-related mortality (IPCC, 2014). These effects are intensified by urbanisation through changes in land surface and anthropogenic activities, influencing the heat storage and fluxes (Oke, 1995). This leads to modifications in cloud cover, precipitation, solar irradiation, air temperature, and wind speed (Kleerekoper et al., 2012). The increased air temperatures in urban areas compared to the surrounding rural areas are referred to as the urban heat island (UHI) effect and is one of the most known and well-documented examples of anthropogenic modifications of the urban atmosphere (Oke, 1973). In 2018, a steadily increasing majority of 55 % of the world's population lived in cities, thereby being exposed to additional thermal stress (Fernandez Milan & Creutzig, 2015; United Nations, Department of Economic and Social Affairs, 2019; Ward et al., 2016).

A growing number of studies show that the intensity, frequency, and duration of heat waves are significantly associated with mortality (Baccini et al., 2008; Le Tertre et al., 2006; Muthers et al., 2017). In Switzerland, the heat wave in summer 2003 led to an increase in excess deaths of 7 % or 1000 fatalities. Large urban areas in France faced over 78 % more fatalities than rural surroundings in record 2003 (Kovats & Kristie, 2006). The summers of 2018 and 2019, during which the heat waves in this study took place, led to an excess mortality in Switzerland of 200 and 500 fatalities, respectively (Bundesamt für Umwelt, 2019; Ragettli & Röösli, 2020).

In order to assess the risks of heat waves in the particularly affected urban areas, knowledge about air temperature distributions within cities are necessary at high spatial resolutions (Hollósi et al., 2021). In addition to direct measurements of air temperatures, which require substantial financial or personnel effort, urban climate models (UCM) are a more cost-effective alternative to assess air temperature patterns in cities. Thus, UCMs can provide an important contribution to the implementation of adaption measures against heat stress in urban planning. In contrast to direct measurements, UCMs can be used to model intended urban planning measures in advance to estimate the resulting benefits.

Numerous studies have already applied MUKLIMO_3 to model the air temperature field of heat waves in urban areas. Often, only a single day or a few days at the peak of the respective heat wave were modelled (e.g., Feranec et al., 2019; Geletič et al., 2018; Holec et al., 2020; Kopecká et al., 2021; Matsaba et al., 2020; Straka & Sodoudi, 2019). The validation could only

be carried out using a few individual air temperature measurement sites in the urban area. However, since heat waves can vary considerably, it is important not to limit the analysis to individual days in single heat waves, but to compare several heat waves over their entire duration with high resolved in-situ data to perform fine-scale evaluations of air temperature distributions within the urban area.

The aim of this study is to fill this gap by applying MUKLIMO_3 to model air temperature patterns throughout three heat waves in 2018 and 2019 for the greater area of Bern, Switzerland. The results will be compared, evaluated, and verified using data from a high-resolution air temperature measurement network within the study area (Gubler et al., 2021). Further, the extent to which the performance of the UCM differs throughout the different heat waves is investigated. For this purpose, differences between MUKLIMO_3 outputs are examined temporally (diurnal cycle), spatially (measurement network sites), and meteorologically (wind patterns and cold air advection).

# 2. Data and methods

## 2.1 Study area

The city of Bern is located at the boundary of the Bernese Pre-Alps and the Swiss Plateau in the western part of Switzerland at 46° 56’ N, 7° 26’ E at an average elevation of 550 m a.s.l. (Fig. 1). The topography of Bern and its surroundings were shaped by glaciers of the last ice age and fluvial erosion of the river Aare and are consequently complex. The Aare flows through Bern from the southeast to the northwest, thus exerting its microclimatic influence on the city. Various hills around the city contribute to the city’s regional and local climate. The highest elevation in the immediate vicinity is Bantiger in the northeast with an altitude of 947 m a.s.l. Several valleys lead to thermotopographic wind systems at different scales. With 134’000 inhabitants in the city and 400’000 in its greater metropolitan area, Bern is the fifth largest city of Switzerland (BFS & Schweizerischer Städteverband, 2020).

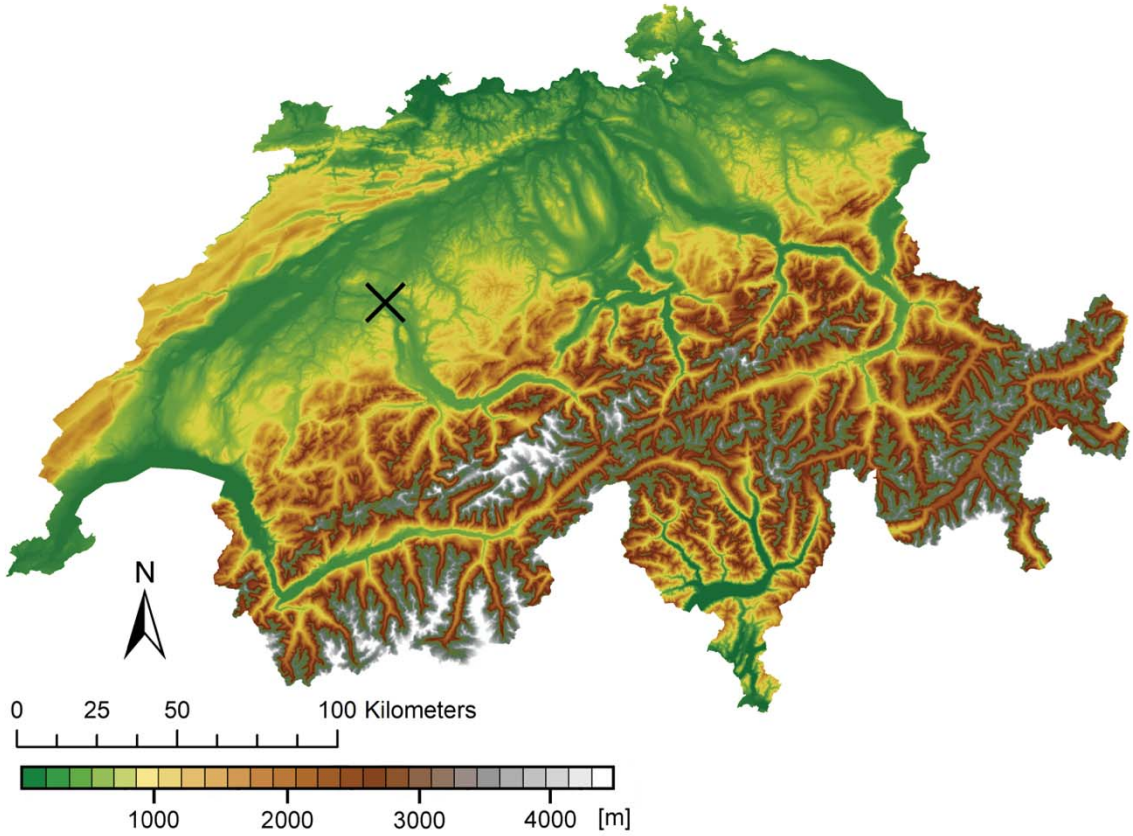


**Fig. 1.** Topography of Switzerland based on the digital elevation model swissALTI$^{3D}$ (swisstopo, 2018). The black cross indicates the location of Bern (46° 56' N, 7° 26' E).

## 2.2 General climatology of Bern

According to the Köppen Climate Classification, Bern has a warm temperate, fully humid climate with warm summers (Cfb) (Kottek et al., 2006). The rural WMO-certified weather station Bern/Zollikofen, which is located about 5 km north of the city centre, experienced an annual mean temperature of 8.8 °C, and an average annual precipitation of 1059 mm for the reference period 1981-2010. The monthly average of all daily maximum temperatures in the months June, July and August were 21.7 °C, 24.3 °C and 23.8 °C, respectively. The monthly average of all daily minimum temperatures in summer were 10.5 °C, 12.5 °C and 12.3 °C, respectively. The average annual amount of heat days ($T_{max} \geq 30$ °C) is 6.3, the number of tropical nights ($T_{min} \geq 20$ °C) is 0 (MeteoSwiss, 2020a). The monthly precipitation amounts in summer were 111 mm, 106 mm, and 116 mm, respectively (MeteoSwiss, 2020a). The wind conditions on the Swiss Plateau, and thus also around Bern, are characterised by the gradient winds modified by the relief of the main Alpine ridge. Winds from the north to northeast and west to southwest dominate (Mathys et al., 1980).

## 2.3 Heat waves 2018 / 2019

The two summers of 2018 and 2019 recorded the fourth and third hottest summers in Switzerland since measurements began in 1864, with nationally averaged summer air temperature being 2.0 K and 2.1 K above the 1981-2010 norm, respectively. In addition, Bern/Zollikofen experienced above-average sunshine duration (129 % and 120 %) and below-average precipitation (76 % and 84 %) (MeteoSwiss, 2018, 2020b). Both summers were characterised by exceptionally long or intense heat waves.

MeteoSwiss defines a heat wave as a period of extreme heat stress that can endanger human health. Until May 2021, official heat warnings from MeteoSwiss were based on a calculated quantity of temperature and relative humidity: the so-called Heat Index (HI) (MeteoSwiss, 2019). The HI is calculated with the formula of Rothfusz (1990) using the daily maximum air temperature and relative humidity at Bern/Zollikofen. A heat wave is defined as a period of at least three days with HI > 90 (danger level 3, significant danger) and an extreme heat wave as a period of at least five days with HI > 93 (danger level 4, severe danger).

For this study, three extreme heat waves were identified in 2018 and 2019 for Bern/Zollikofen (Tab. 1): In 2018, the extreme heat wave started on 30 July and lasted for 10 days until 8 August (HW18). 2019 was represented by two extreme heat waves, whereas the first one lasted from 24 June to 1 July (HW19.1) and the second one from 22 July to 26 July (HW19.2). Since an extreme heat wave must have HI > 93 for at least five days, and in HW19.2 the first day had an HI of 92.8, this heat wave cannot, strictly speaking, be called an extreme heat wave (Fig. 2). However, as maximum HI values reach up to 107.9, this heat wave is still considered an extreme heat wave in this study (MeteoSwiss, 2019).

The wind field in Bern/Zollikofen, measured at 10 m above ground, shows a similar diurnal cycle over all three heat waves investigated (Fig. 3). During the day, winds from the north to north-east predominate, while at night winds from the south to south-west are more frequent. The wind field on Bantiger, measured at 155 m above ground, shows almost constant wind from the north-east for HW18 over the entire diurnal cycle (Fig. 4). During HW19.1, wind is also mainly from the north-east during the day. In the first half of the night there is on average more wind from the south and until the early morning wind from the southwest dominates. In HW19.2, north-easterly winds are predominant during the day and the first half of the night, while south-westerly winds dominate the second half of the night.

**Tab. 1.** Measured values for the three extreme heat waves under investigation in Bern/Zollikofen. $\mathbf{T_{avg}}$ shows the average daily air temperature, $\mathbf{T_{max}}$ the average daily maximum air temperature, $\mathbf{T_{min}}$ the average daily minimum air temperature, $\mathbf{HI_{avg}}$ the average daily heat index value, and $\mathbf{T_w}$ the average water temperature of Aare at the station Schönau (Federal Office for the Environment, 2021; MeteoSwiss, 2021)

| Heat wave | Duration | $T_{avg}$ | $T_{max}$ | $T_{min}$ | $HI_{avg}$ | $T_w$ |
|---|---|---|---|---|---|---|
| HW18 | 10 days | 24.2 °C | 32.2 °C | 16.8 °C | 101.6 | 21.9 °C |
| HW19.1 | 8 days | 25.0 °C | 32.2 °C | 16.4 °C | 101.9 | 17.8 °C |
| HW19.2 | 5 days | 25.2 °C | 33.3 °C | 16.6 °C | 103.0 | 21.1 °C |

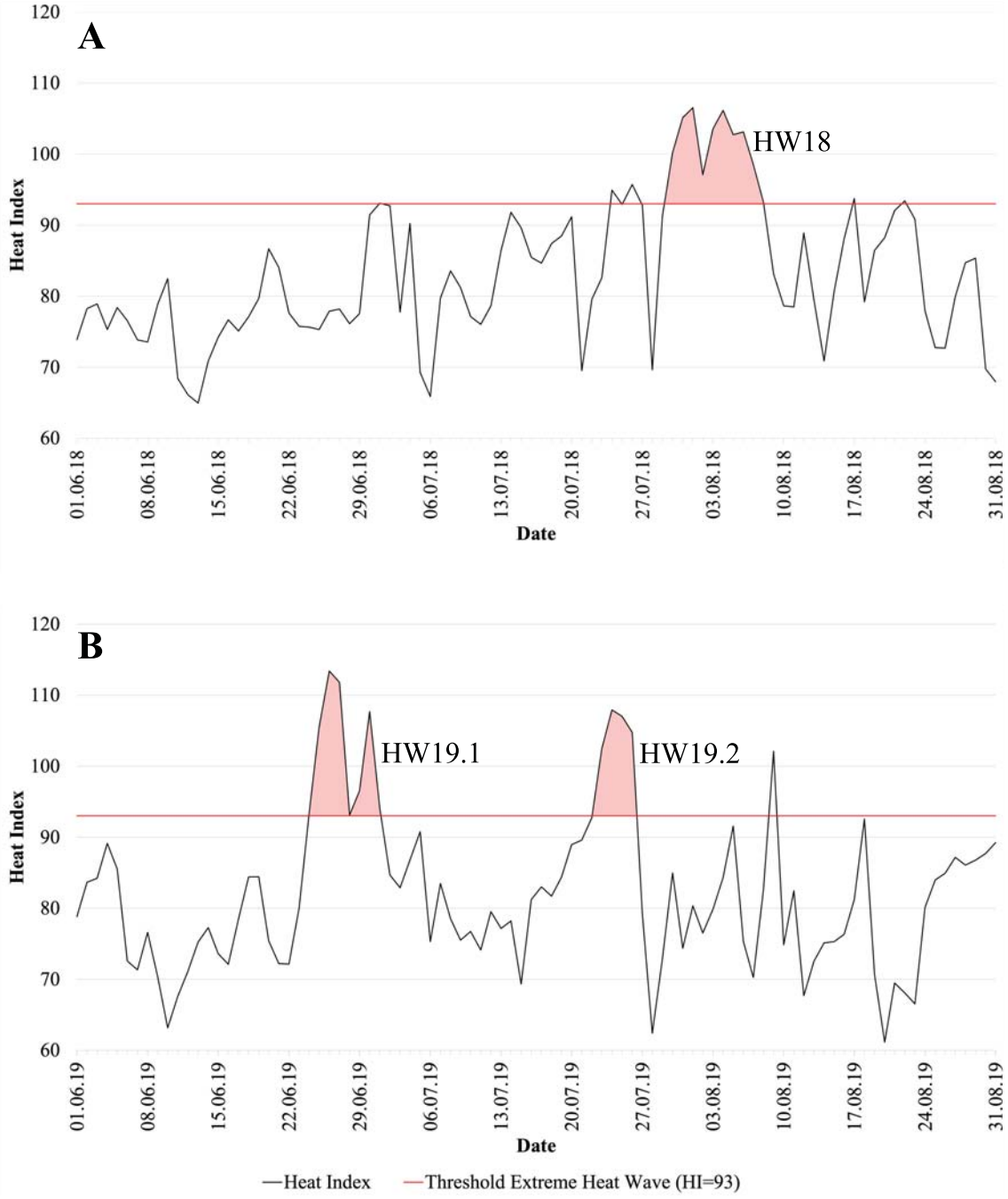


**Fig. 2.** Heat index in Bern/Zollikofen during summer 2018 (**A**) and summer 2019 (**B**). The horizontal red line represents the threshold for extreme heat waves (HI = 93). Marked are the three extreme heat waves HW18, HW19.1, and HW19.2.

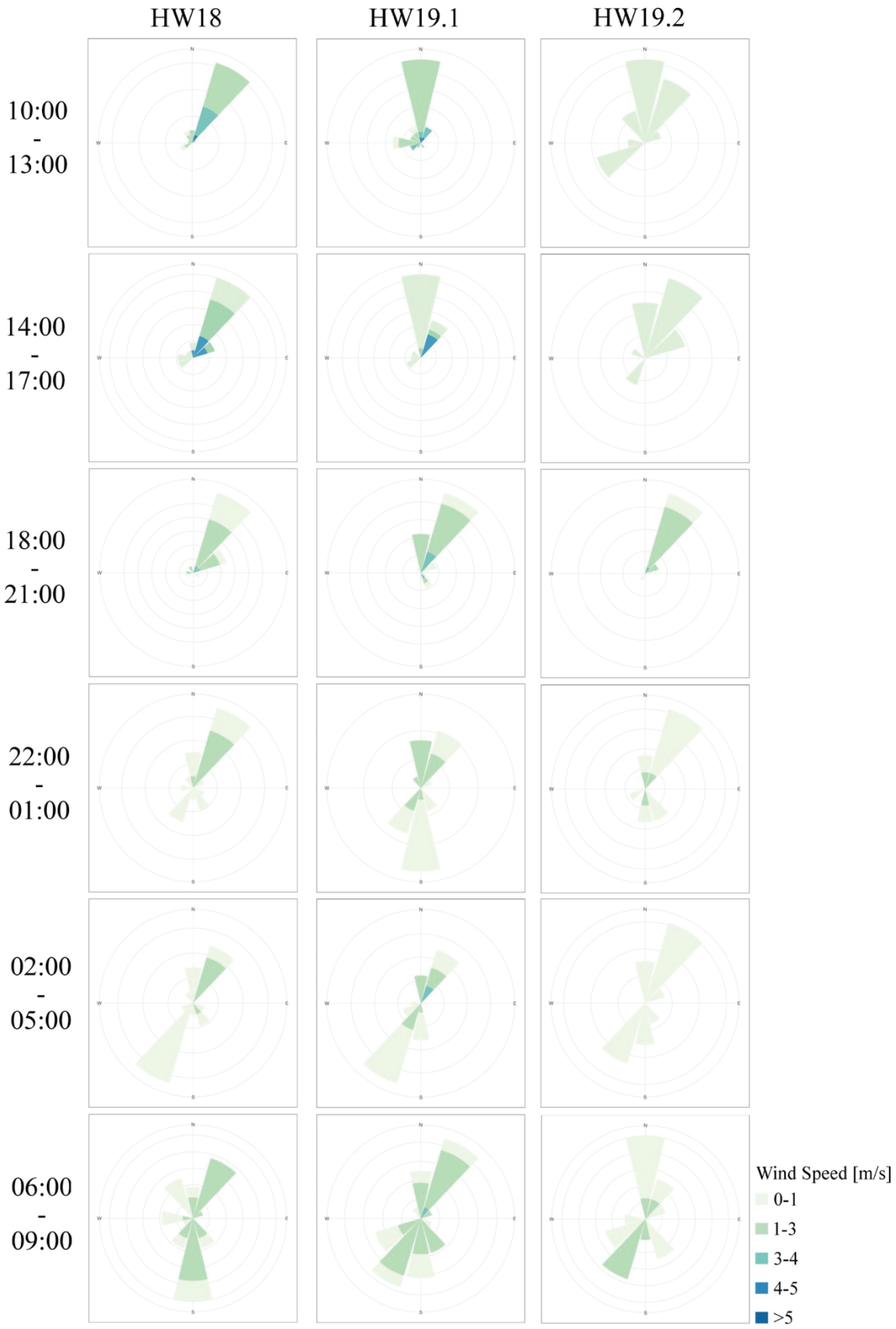


**Fig. 3.** Wind roses showing average wind speed and direction for HW18, HW19.1, and HW19.2 for 10:00-13:00, 14:00-17:00, 18:00-21:00, 22:00-01:00, 02:00-05:00, and 06:00-09:00 CEST (Central European Summer Time, UTC+2) for the measurement site Bern/Zollikofen at 10 m above ground. The length of the flag corresponds to the relative frequency per wind direction. Hours with rain and subsequent hours of the respective model run are not included as described in Section 2.4.3.

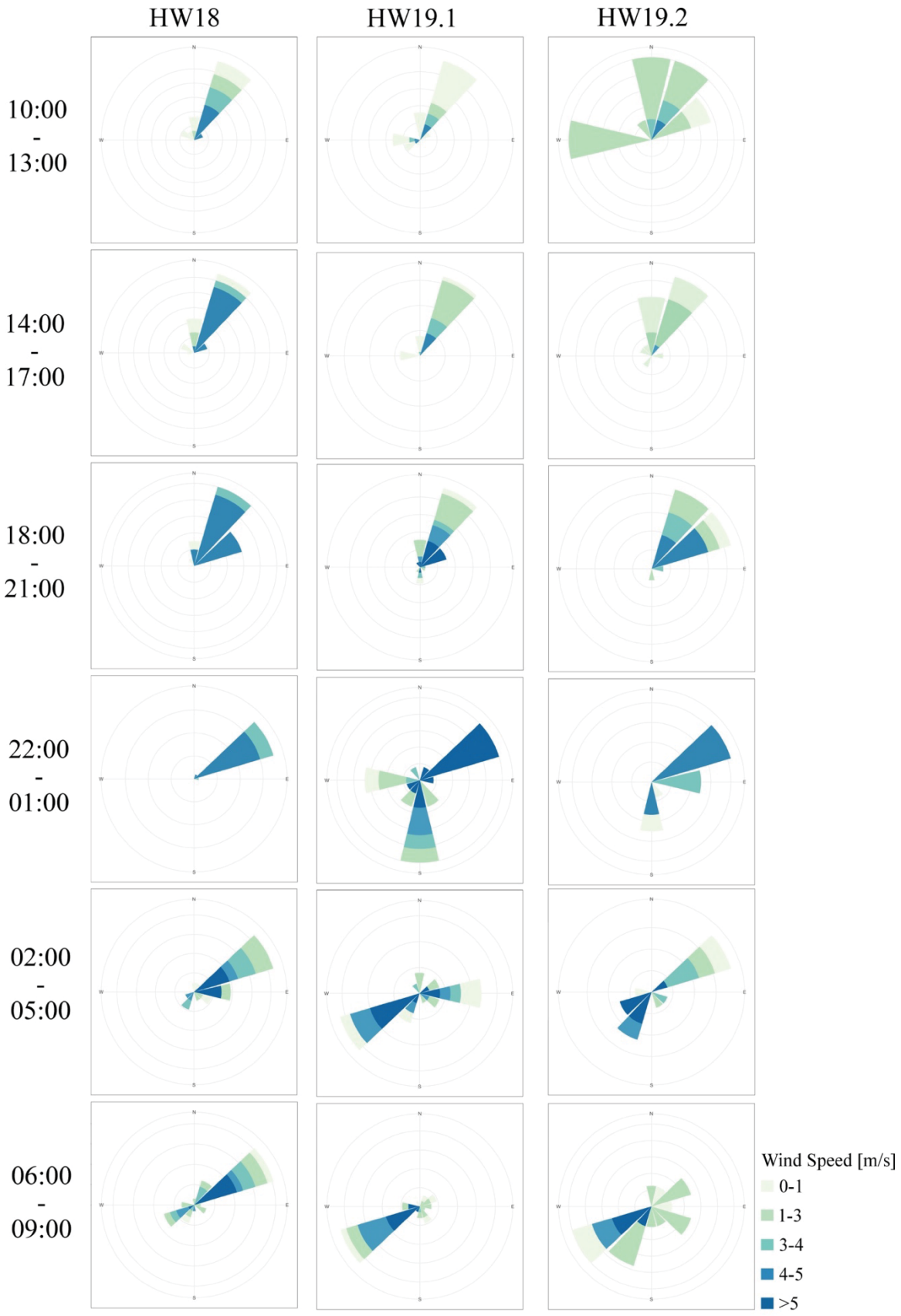


**Fig. 4.** Wind roses showing average wind speed and direction for HW18, HW19.1, and HW19.2 for 10:00-13:00, 14:00-17:00, 18:00-21:00, 22:00-01:00, 02:00-05:00, and 06:00-09:00 CEST for the measurement site Bantiger at 155 m above ground. The length of the flag corresponds to the relative frequency per wind direction. Hours with rain and subsequent hours of the respective model run are not included as described in Section 2.4.3.

## 2.4 MUKLIMO_3

To simulate diurnal cycles of atmospheric variables (temperature, moisture, wind field, radiation) on a three-dimensional model grid in dependence on prevailing weather conditions, land use, and topography, the non-hydrostatic microscale UCM MUKLIMO_3 (3-dimensionales mikroskaliges urbanes Klimamodell) developed by the German Weather Service in 1986 and continuously improved and extended until the current version of June 2020 (v200629) was used (Sievers, 2016).

During a model run, two phases can be distinguished: First, the one-dimensional drive model (1D) runs alone for a certain time in order to calculate the initial conditions with the help of given input factors (Sievers, 2016). Then the three-dimensional simulation (3D) starts, with 1D continuing to run in parallel and providing the upper boundary values for 3D. The lateral sides of 3D have free boundary conditions with horizontal advection terms being zero at the upstream domain boundaries (Žuvela-Aloise, 2017). Both 1D and 3D include atmospheric balance equations for wind, air temperature and specific humidity, balance equations for temperature and volumetric water content in the earth's soil, and an interface model of the earth's surface that also takes vegetation into account and connects the atmosphere with the earth's soil (Siebert et al., 1992; Sievers et al., 1983; Sievers & Zdunkowski, 1986). In addition, there are model equations for calculating the incoming short-wave and long-wave radiant flux densities on the surfaces. Unlike 3D, 1D requires horizontal homogeneity and does not include buildings or trees.

In order to reduce the computational effort to investigate entire cities, the air flow in built-up area is parametrized through a porous medium for unresolved buildings, characterized by the building height and wall area within each grid cell (Gross, 1989). To carry out a simulation, datasets on topography and description of land use classes (LUC, further description in Section 2.6) within the model area are required. Moreover, the meteorological situation at the start of the simulation is described by measured soil temperature in 1 m depth, as well as air temperature and relative humidity at up to five different altitudes. The water temperature, the temperature inside the buildings, and the degree of cloud cover are fixed over the whole simulation. The wind speed and direction show a diurnal cycle and are defined for each individual daytime hour.

### 2.4.1 Land use classes

Besides topography, MUKLIMO_3 requires detailed information about the land use of each grid cell. The definition of LUCs is primarily conducted using the dataset "Amtliche Vermessung vereinfacht", which contains the most accurate geodata available for the Canton of Bern (Amt für Geoinformation des Kantons Bern, 2021; Tab. 2). The dataset swissBUILDINGS$^{3D}$ 2.0 (swisstopo, 2021) is used to subdivide the buildings according to their area, Imperviousness Density 2018 (European Environment Agency, 2020a) to subdivide roads and squares according to the degree of sealing and Ginzler & Hobi (2015) to subdivide garden areas according to the vegetation height. Using these datasets, 23 LUCs are defined, which are as optimally delineated from each other and as homogenous within themselves as possible (Fig. 5D).

Each class is described by 26 physical parameters, which contain information about building and vegetation characteristics as well as the degree of soil sealing (Tab. 3). All parameters are determined for a grid cell size of 50 x 50 m and averaged over all grid cells of the model area. The building parameters "building fraction of the first building type" (vg1), "wall area index of the first building type" (wai1) and "mean building height of the first building type" (h1) are derived using swissBUILDINGS$^{3D}$ 2.0. For simplicity, all buildings are combined into one building type and a possible second building type (vg2, wai2, h2) is omitted. "Fraction of impervious surface between buildings" (vs) refers to the proportion of the surface area that is unbuilt and is determined with Imperviousness Density 2018. "Surface roughness of the non-built-up areas or areas below trees" (z0 in m) could not be determined with the available datasets, therefore, after consultation with the German Weather Service and the Central Institution for Meteorology and Geodynamics (ZAMG), a surface roughness of 0.2 is estimated for the non-built-up areas of grid cells with buildings or trees and 0.1 for the non-built-up areas of all other grid cells. "Tree height" (hbm in m) and "stem height" (hst in m) is determined using Ginzler & Hobi (2015), assuming half the tree height for the stem height and reducing the stem height by 2 m for large trees over 20 m. "Leaf area density in the tree top area" (bf0 in $m^{-1}$) and "leaf area density in the stem area" (bf1 in $m^{-1}$) has been set to 0.05 $m^{-1}$ and 0.8 $m^{-1}$, respectively. "Leaf area index of the canopy layer" (lai, dimensionless) is set to 1.5 for forests and close to 1 for all other LUCs. "Vegetation height of the canopy layer" (hca in m) is determined for grid cells without tree cover by Ginzler & Hobi (2015). In the case of tree cover, the vegetation height in Ginzler & Hobi (2015) corresponds to the tree height, therefore the vegetation height of the canopy layer is estimated to 0.4 m to 0.7 m.

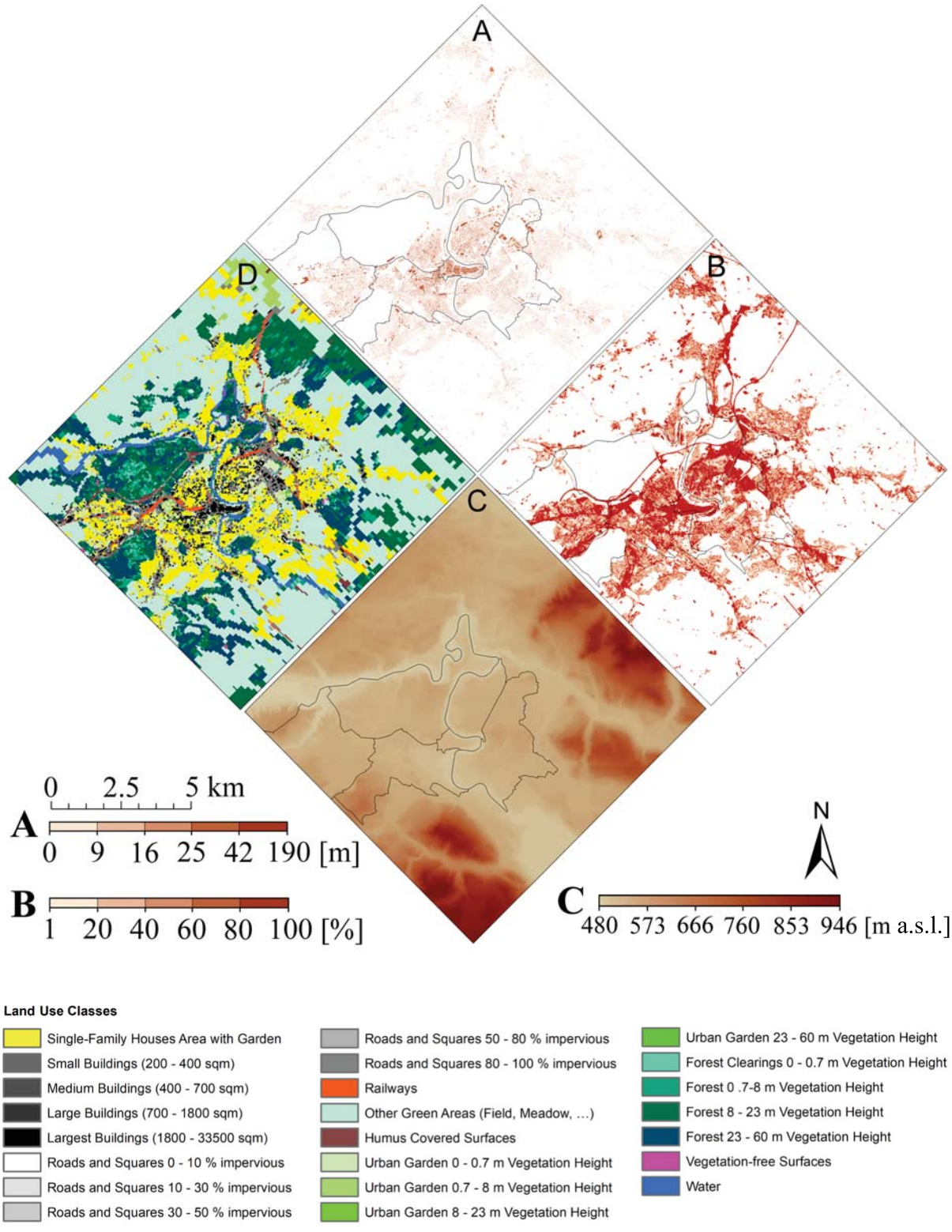


**Fig. 5.** Information for model input data: **A** shows the building height based on swissBUILDINGS$^{3D}$ 2.0 (swisstopo, 2021), **B** the fraction of impervious surfaces based on Imperviousness Density 2018 (European Environment Agency, 2020a), **C** the digital elevation model based on swissALTI$^{3D}$ (swisstopo, 2018), and **D** the self-defined LUCs with the table below. Solid black lines show the city districts of Bern.

"Tree cover" (sigbm, dimensionless) is determined as the vertical projection of tree crowns to a horizontal earth's surface using Tree Cover Density 2018 (European Environment Agency, 2020b). "Vegetational cover of the canopy layer" (sigma, dimensionless) is determined using "Amtliche Vermessung vereinfacht". All other parameters have not been adjusted and are therefore set with default values by MUKLIMO_3 (DWD, 2020; Sievers, 2012). Buildings (vg1) and trees (sigbm) cannot occur in the same grid cell, so in each LUC the dominant factor is determined and the respective is ignored.

**Tab. 2.** Defined LUCs. The left column contains the datasets used, which are summarised with the LUCs in the right column. swissBUILDINGS$^{3D}$ 2.0 (swisstopo, 2021) was used for LUC 1 to 5, "Amtliche Vermessung vereinfacht" (Amt für Geoinformation des Kantons Bern, 2021) for LUC 1 and 6 to 23, Imperviousness Density 2018 (European Environment Agency, 2020a) for LUC 6 to 10 and Ginzler & Hobi (2015) for LUC 14 to 21. The following German (with English translations) abbreviations were used for the left column: St (Strasse - street), T (Trottoir - pavement), V (Verkehrsinsel – traffic island), FP (Flugplatz – air field), üb (übrige befestigte – other paved), vh (Vegetationshöhe - vegetation height), F (Fels - rock), G (Geröll - boulders), S (Sand - sand), A (Abbau - mining), D (Deponie - landfill), üv (übrige vegetationslose – other vegetationless), W (Wasserbecken – water basin), fG (fliessendes Gewässer – stretch of running water), sG (stehendes Gewässer – stretch of standing water), S (Schilfgürtel – reed belt). Additional German expressions are Bahn (Railway), Acker (field), Wiese (meadow), Reben (vines), übrige Intensivkulturen (other intensive crops), übrige humusierte (other humus), Gartenanlage (garden area), geschlossener Wald (closed forest), and übrige bestockte (remaining stocked)

| **Original Data** | **Land Use Classes** |
|---|---|
| Buildings and Gartenanlage within 10 m radius | 1 Single-Family Houses with Garden |
| Buildings (200-400 $m^2$) | 2 Small Buildings |
| Buildings (400-700 $m^2$) | 3 Medium Buildings |
| Buildings (700-1800 $m^2$) | 4 Large Buildings |
| Buildings (1800-33500 $m^2$) | 5 Largest Buildings |
| St, Weg, T, V, FP, üb (0-10 % impervious) | 6 Roads and Squares 0-10 % impervious |
| St, Weg, T, V, FP, üb (10-30 % impervious) | 7 Roads and Squares 10-30 % impervious |
| St, Weg, T, V, FP, üb (30-50 % impervious) | 8 Roads and Squares 30-50 % impervious |
| St, Weg, T, V, FP, üb (50-80 % impervious) | 9 Roads and Squares 50-80 % impervious |
| St, Weg, T, V, FP, üb (80-100 % impervious) | 10 Roads and Squares 80-100 % impervious |
| Bahn | 11 Railways |
| Acker, Wiese, Reben, übrige Intensivkulturen | 12 Other Green Areas |
| übrige humusierte | 13 Humus Covered Surfaces |
| Gartenanlage (0-0.7 m vh) | 14 Urban Garden 0-0.7 m Vegetation Height |
| Gartenanlage (0.7-8 m vh) | 15 Urban Garden 0.7-8 m Vegetation Height |
| Gartenanlage (8-23 m vh) | 16 Urban Garden 8-23 m Vegetation Height |
| Gartenanlage (23-60 m vh) | 17 Urban Garden 23-60 m Vegetation Height |
| geschlossener Wald, übrige bestockte (0-0.7 m vh) | 18 Forest Clearings 0-0.7 m Vegetation Height |
| geschlossener Wald, übrige bestockte (0.7-8 m vh) | 19 Forest 0.7-8 m Vegetation Height |
| geschlossener Wald, übrige bestockte (8-23 m vh) | 20 Forest 8-23 m Vegetation Height |
| geschlossener Wald, übrige bestockte (23-60 m vh) | 21 Forest 23-60 m Vegetation Height |
| F, G, S, A, D, üv | 22 Vegetation-free Surfaces |
| W, fG, sG, S | 23 Water |

**Tab. 3.** Physical parameters used for the individual LUCs. The fraction of impervious surface between buildings (vs) for water (LUC=23) is set to -1 by convention. Only the first 16 parameters are shown, as the other parameters are used for measures such as green roofs, changed albedo of walls, roofs or surfaces or a changed heat capacity. For this study, these were filled with model internal default values

| LUC | vg1 | vg2 | wai1 | wai2 | h1 | h2 | vs | z0 | hbm | hst | bf0 | bf1 | lai | hca | sigbm | sigma |
|---|---|---|---|---|---|---|---|---|---|---|---|---|---|---|---|---|
| 1 | 0.32 | 0 | 1.7 | 0 | 13.21 | 0 | 0.41 | 0.2 | 0 | 0 | 0 | 0 | 0.8 | 0.4 | 0 | 0.40 |
| 2 | 0.37 | 0 | 1.7 | 0 | 11.38 | 0 | 0.51 | 0.2 | 0 | 0 | 0 | 0 | 0.8 | 0.4 | 0 | 0.40 |
| 3 | 0.41 | 0 | 1.8 | 0 | 12.92 | 0 | 0.60 | 0.2 | 0 | 0 | 0 | 0 | 1.0 | 0.5 | 0 | 0.46 |
| 4 | 0.44 | 0 | 0.9 | 0 | 15.87 | 0 | 0.72 | 0.2 | 0 | 0 | 0 | 0 | 1.0 | 0.4 | 0 | 0.40 |
| 5 | 0.63 | 0 | 2.1 | 0 | 20.81 | 0 | 0.86 | 0.2 | 0 | 0 | 0 | 0 | 0.9 | 0.4 | 0 | 0.44 |
| 6 | 0 | 0 | 0 | 0 | 0 | 0 | 0.00 | 0.1 | 7.2 | 3.6 | 0.05 | 0.8 | 0.8 | 1.0 | 0.2 | 0.39 |
| 7 | 0 | 0 | 0 | 0 | 0 | 0 | 0.24 | 0.1 | 5.7 | 2.8 | 0.05 | 0.8 | 0.8 | 1.0 | 0.2 | 0.39 |
| 8 | 0 | 0 | 0 | 0 | 0 | 0 | 0.40 | 0.1 | 3.0 | 1.5 | 0.05 | 0.8 | 0.8 | 1.0 | 0.1 | 0.39 |
| 9 | 0 | 0 | 0 | 0 | 0 | 0 | 0.66 | 0.1 | 0 | 0 | 0 | 0 | 0.8 | 1.6 | 0.1 | 0.39 |
| 10 | 0 | 0 | 0 | 0 | 0 | 0 | 0.97 | 0.1 | 0 | 0 | 0 | 0 | 0.8 | 0.5 | 0 | 0.39 |
| 11 | 0 | 0 | 0 | 0 | 0 | 0 | 0.80 | 0.1 | 0 | 0 | 0 | 0 | 0.9 | 0.5 | 0.1 | 0.39 |
| 12 | 0 | 0 | 0 | 0 | 0 | 0 | 0.01 | 0.1 | 0 | 0 | 0 | 0 | 1.0 | 0.7 | 0.1 | 0.99 |
| 13 | 0 | 0 | 0 | 0 | 0 | 0 | 0.29 | 0.1 | 3.2 | 1.6 | 0.05 | 0.8 | 0.8 | 0.5 | 0.2 | 0.39 |
| 14 | 0 | 0 | 0 | 0 | 0 | 0 | 0.36 | 0.2 | 0 | 0 | 0 | 0 | 0.9 | 0.4 | 0 | 0.72 |
| 15 | 0 | 0 | 0 | 0 | 0 | 0 | 0.28 | 0.2 | 0 | 0 | 0 | 0 | 0.9 | 0.4 | 0 | 0.89 |
| 16 | 0 | 0 | 0 | 0 | 0 | 0 | 0.18 | 0.2 | 11.2 | 5.6 | 0.05 | 0.8 | 0.9 | 0.4 | 0.2 | 0.89 |
| 17 | 0 | 0 | 0 | 0 | 0 | 0 | 0.07 | 0.2 | 23.5 | 9.7 | 0.05 | 0.8 | 0.9 | 0.4 | 0.2 | 0.89 |
| 18 | 0 | 0 | 0 | 0 | 0 | 0 | 0.02 | 0.2 | 2.7 | 1.4 | 0.05 | 0.8 | 1.5 | 1.0 | 0.6 | 0.76 |
| 19 | 0 | 0 | 0 | 0 | 0 | 0 | 0.00 | 0.2 | 5.0 | 2.5 | 0.05 | 0.8 | 1.5 | 1.0 | 0.9 | 0.76 |
| 20 | 0 | 0 | 0 | 0 | 0 | 0 | 0.00 | 0.2 | 15.6 | 7.8 | 0.05 | 0.8 | 1.5 | 1.0 | 0.6 | 0.76 |
| 21 | 0 | 0 | 0 | 0 | 0 | 0 | 0.00 | 0.2 | 28.9 | 12.5 | 0.05 | 0.8 | 1.5 | 1.0 | 0.6 | 0.76 |
| 22 | 0 | 0 | 0 | 0 | 0 | 0 | 0.12 | 0.1 | 5.7 | 2.8 | 0.05 | 0.8 | 1.0 | 0.4 | 0.2 | 0.12 |
| 23 | 0 | 0 | 0 | 0 | 0 | 0 | -1 | 0.001 | 0 | 0 | 0 | 0 | 0 | 0 | 0 | 0 |

## 2.4.2 Nesting

To achieve the highest possible spatial resolution at ground level and in the central parts of the city, a three-dimensional nesting is implemented. For this purpose, the horizontal nesting illustrated in Fig. 6 is used. The core area of the city of Bern, including the immediate surrounding area, is modelled with the highest possible spatial resolution of 50 x 50 m. A higher resolution is theoretically possible, but the fraction of buildings per grid cell (vg1) should not exceed 0.75, which is then no longer guaranteed (DWD, 2020). The grid cell spacing increases continuously towards the city's periphery to 200 m, whereby neighbouring grid cells differ by a maximum factor of 1.3 to avoid numerical instabilities in the model. In the vertical direction, the grid cell spacing is increased with increasing height from 10 m to 100 m in 53 levels over the entire model area. This allows the layers close to the ground to be optimally mapped and

the influence of the overlying atmosphere to be included using as few computing resources as possible. These properties lead to a model area with 202 x 173 x 53 grid cells in northeast, northwest, and vertical direction, respectively.

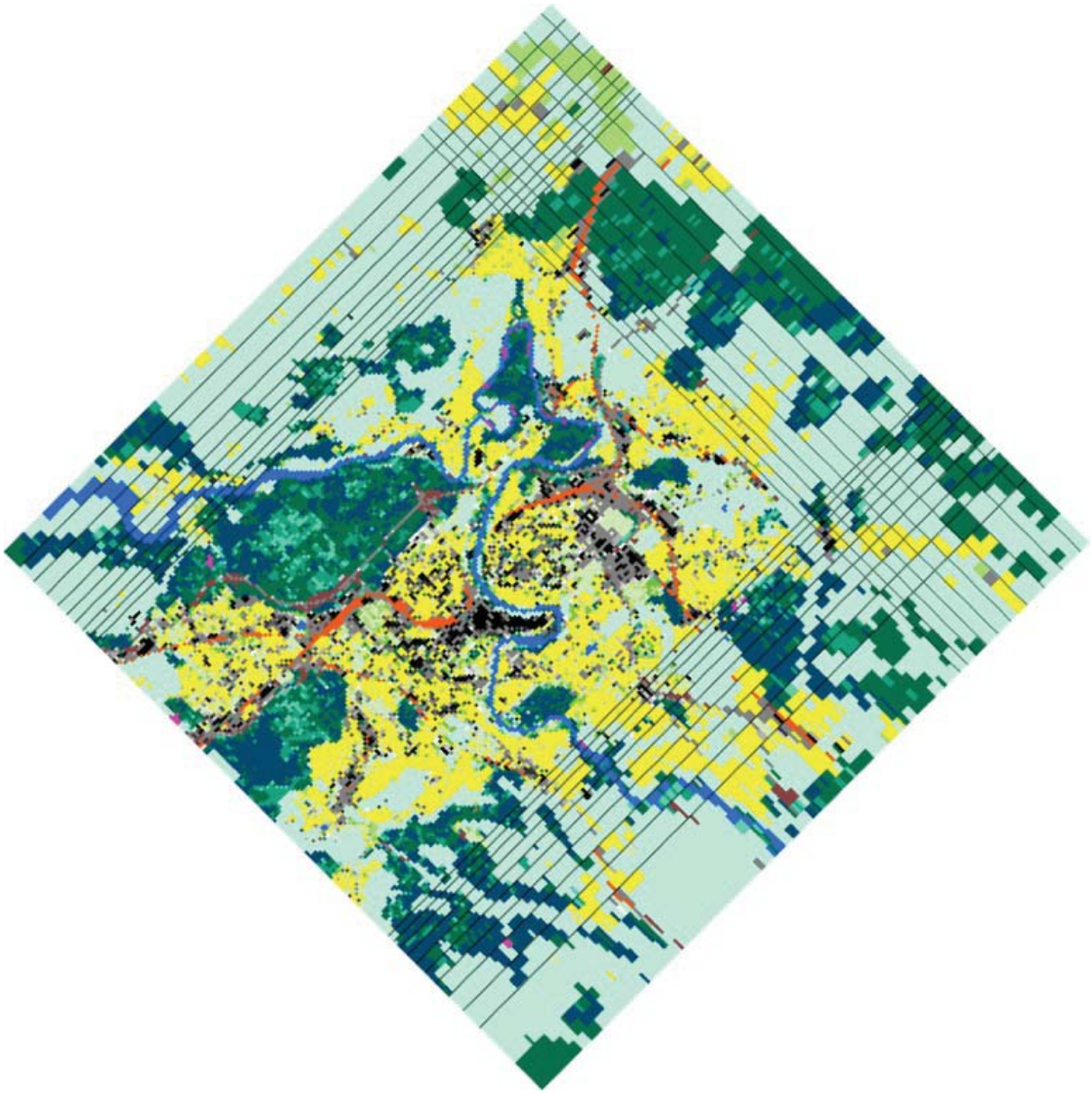

**Fig. 6.** Implemented nesting in horizontal direction with the LUCs described in Fig. 3. The black lines show the transition from one grid cell spacing to the next.

### 2.4.3 Modelling approach

The model area has a horizontal extent of 12.1 x 12.1 km and is rotated by 45° against north, which allows relevant topographic features in the vicinity of Bern to be included. The vertical extent corresponds to 1611 m, with the model area being based on the lowest point of the area (Wohlensee, 480 m a.s.l.). Thus, the model top reaches a height of 2091 m a.s.l., so that all surrounding mountains and their influence on the overlying atmosphere are represented.

The start time of the MUKLIMO_3 simulations should be chosen so that the influence of the LUCs is as small as possible at the beginning. This is determined by the smallest average variance of the high-resolution air temperature measurement network by Gubler et al. (2021) during each diurnal cycle of all the heat waves. Therefore, 3D was started for each individual day at 07:00 CEST (Central European Summer Time, UTC+2) and modelled over 25 h. This allowed a complete diurnal cycle to be generated while removing the first hour (remaining data from 08:00 CEST to 07:00 CEST the following day), as this is used to create steady-state profiles of the atmospheric and ground variables. For this, 1D ran from 07:00 CEST to 07:00 CEST the following day to provide initial conditions for 3D.

Since MUKLIMO_3 cannot represent phase transitions of water vapour in the atmosphere, and thus neither cloud formation nor rain or snow, precipitation periods as well as the following hours of the respective model run were excluded from further investigations (Sievers, 2016). As precipitation during the heat waves often occurred in the form of small-scale thunderstorms that did not affect the entire model area, radar images were used to determine when a precipitation event occurred inside the model area (Kachelmannwetter, 2021). Thereby, the entire model area of the time periods shown in Tab. 4 was excluded from further investigations. A total of 146 / 240 hours (61 %) remain in HW18, 168 / 192 hours (88 %) in HW19.1, and 88 / 96 (92 %) hours in HW19.2.

**Tab. 4.** Periods excluded from further investigations due to precipitation. The times are given in CEST

| **HW18** | **HW19.1** | **HW19.2** |
|---|---|---|
| 01.08.18 16:00 – 02.08.18 07:00 | 01.07.19 00:00 – 01.07.19 07:00 | 26.07.19 00:00 – 26.07.19 07:00 |
| 04.08.18 17:00 – 05.08.18 07:00 | 01.07.19 16:00 – 02.07.19 07:00 | |
| 06.08.18 17:00 – 09.08.18 07:00 | | |

## 2.5 High-resolution air temperature network in Bern

To validate the modelled air temperature distribution in the greater area of Bern, these are compared with measured air temperature data. From May to September 2018 and 2019, a low-cost air temperature measurement network was in operation to assess fine-scale spatiotemporal air temperature variability across the city of Bern and its surroundings using 79 (2018) and 84 (2019) thermistor-based HOBO Pendant® temperature loggers, respectively, whereas 64 loggers were placed at the same locations during both summers (Fig. 7). They were installed at about 3 m above ground to prevent vandalism, which is above standard height of 2 m but acceptable for urban canopy layer temperature measurements (WMO, 2006). Three temperature loggers were installed directly at the existing rural WMO-certified weather station in Bern/Zollikofen, at the suburban weather station of the city's Environmental Protection Office (AfU) at Wankdorf, and at the weather station of the Swiss Federal Laboratories for Materials Science and Technology (EMPA) on the roof of a multi-story building approximately 30 m above street level next to the main train station at Bollwerk. At these sites, data from automated and actively ventilated temperature sensors were used to determine the quality of the low-cost measurements.

The temperature loggers recorded near-surface air temperatures at 10-minutes intervals, but due to the plastic coating of the sensor, the temperature loggers have a relatively long *e*-folding time of 10 min for changes in ambient temperatures (Gubler et al., 2021). Therefore, the hourly outputs of MUKLIMO_3 were compared with the measured air temperature values 10 min later (modelled air temperature at xx:00 was compared with the measured air temperature at xx:10).

### 2.5.1 Temporal evaluation with MUKLIMO_3

The temporal evaluation is based on six specific time steps during the course of the day separated by heat waves (02:00, 06:00, 10:00, 14:00, 18:00, and 22:00 CEST). In each time step, all available loggers were included so that no spatial subdivision was applied to allow the spatial and temporal evaluation to be carried out separately. The fit for the linear regression is determined individually for the six time steps. In addition, the standard deviation, the root mean square error (RMSE), and the Pearson correlation are presented graphically using a Taylor diagram (Taylor, 2001). The scatter of the bias between measured and modelled air temperatures as well as its median is presented using boxplots for all time steps over the entire diurnal cycle. In order to conduct an analysis of the spatial distribution of air temperature for

the six time steps, maps of the UHI, divided by heat wave, were analysed in a qualitative manner. The UHI was defined so that each grid cell reflects the difference to the grid cell with the measurement site Bern/Zollikofen. This allows to determine whether MUKLIMO_3 realistically represents the spatial distribution of air temperature over the course of the day. In addition, it enables modelled cold air drainage from the surrounding elevations to be detected.

### 2.5.2 Spatial evaluation with MUKLIMO_3

The measurement network covers a wide variety of city districts, neighbouring agglomeration, and rural surroundings. To allow a spatial evaluation between the measurement network and MUKLIMO_3, a classification of all measurement sites into different local climate zones (LCZ) was applied. The LCZ concept was introduced by Stewart & Oke (2012) and describes a distinct urban area with more or less homogeneous surface cover, structure, materials, and human activity. Each LCZ has a "characteristic screen-height temperature regime that is most apparent over dry surfaces, on calm, clear nights, and in areas of simple relief" (Stewart & Oke, 2012, p. 1884). The classification of LCZs was done for each measurement site using satellite imagery and GIS data in a qualitative manner by Gubler et al. (2021) and adopted for this study (see Appendix Tab. A1).

The measurement sites were grouped according to the LCZs separated by heat waves and statistically evaluated for all available hours over the entire diurnal cycle. For this purpose, the fit for the linear regression per LCZ was determined over all time steps. Using a Taylor diagram, each individual LCZ is examined separately according to heat wave (Taylor, 2001). The scatter of the bias between measured and modelled air temperatures as well as its median is presented using boxplots per LCZ over all available time steps.

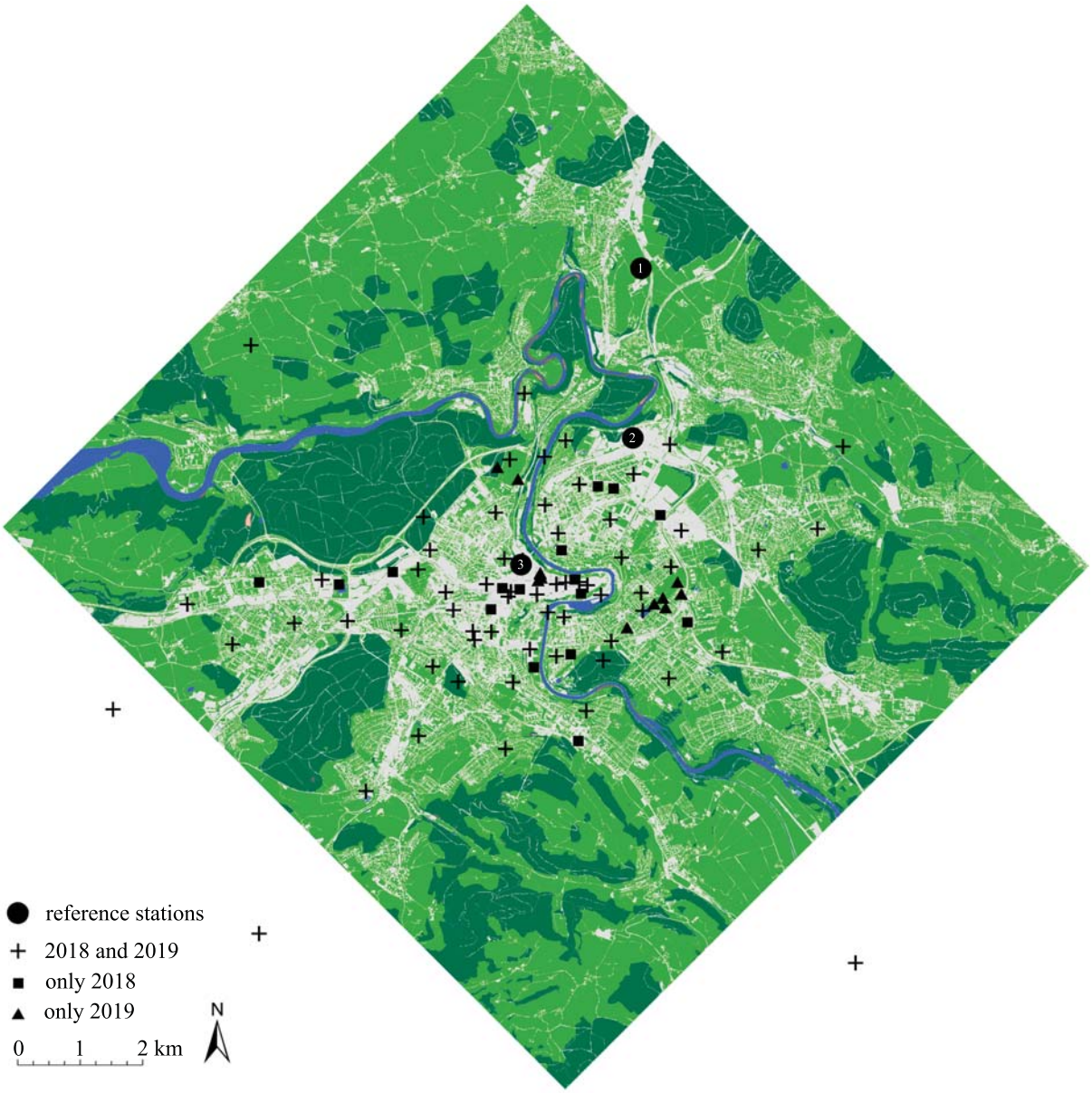


**Fig. 7.** Measurement sites of the high-resolution air temperature measurement network in Bern classified according to operating years 2018 and 2019, and reference stations (operation in both years). ① indicating measurement site Bern/Zollikofen, ② measurement site Wankdorf, and ③ measurement site Bollwerk. Three rural stations are outside the model area and are therefore not considered for this study. Dark green are forests, light green are open green spaces, blue are water areas and light grey are all sealed surfaces.

# 3. Results

## 3.1. Temporal evaluation

The hourly outputs of the air temperature fields at 3 m above ground from MUKLIMO_3 were temporally compared with the low-cost measurement network of Gubler et al. (2021), including all available measurement sites over the entire diurnal cycle separated into respective hours of day for each individual heat wave. The comparison of all three heat waves has shown that the median air temperature 3 m above ground in MUKLIMO_3 is lower during daytime and higher during nighttime compared to the measured air temperatures (Fig. 8A to C). The largest negative median air temperature bias can be found between 16:00 and 18:00 CEST over all heat waves during the hottest time of the day with -3.7 K, -4.1 K, and -4.8 K for HW18, HW19.1, and HW19.2, respectively. The largest positive median air temperature bias can be found between 00:00 and 02:00 CEST over all heat waves with 1.5 K, 2.8 K, and 1.5 K for HW18, HW19.1, and HW19.2, respectively. A diurnal pattern is visible, whereby in the morning the air temperatures are consistently lower in MUKLIMO_3 compared to the measured values. The negative bias increases in the afternoon with rising air temperatures, and with decreasing air temperatures in the evening, the sign of bias turns positive, which denotes higher air temperatures in MUKLIMO_3 compared to the measured values at around 21:00 to 23:00 CEST. During night, the positive bias decreases towards 0 K, so that at sunrise (06:00 to 07:00 CEST) a bias of 0.7 K, 0.2 K, and 0.7 K can be determined for HW18, HW19.1, and HW19.2, respectively.

HW19.1 has a larger spread of air temperature bias over the whole diurnal cycle with standard deviations from 2.4 K at noon to 3.0 K at midnight compared to HW19.2 with 1.7 K at midnight and 1.3 K at noon. HW18 has no specific diurnal cycle with respect to the spread of the air temperature bias between MUKLIMO_3 and measured air temperature. HW19.1 shows a higher RMSE and a similar standard deviation over the entire diurnal cycle compared to HW18 and HW19.2 (Fig. 8D). Especially in HW19.2, high Pearson correlation values of almost 0.9 have been reached during the afternoon, whereas in HW18 and HW19.1 with slightly over 0.6 and 0.4, respectively, these values were substantially lower. The fit of the linear regression shows significantly lower values for HW19.1 over the entire course of the day with 0.07 to 0.18 than in HW18 and HW19.2 with 0.11 to 0.43 and 0.10 to 0.75, respectively (Tab. 5). In general, substantially higher values are achieved during the day than at night over all three heat waves.

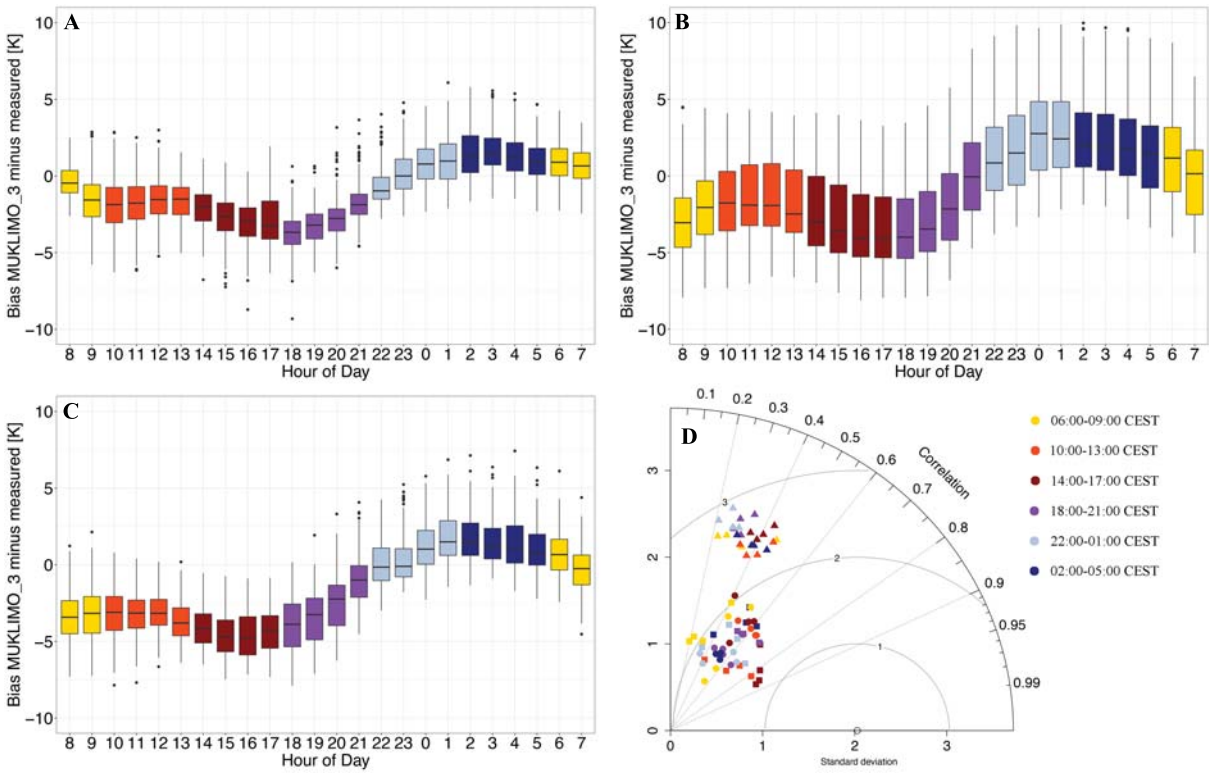


**Fig. 8.** Boxplots of hourly air temperature difference of MUKLIMO_3 at 3 m above ground and the measured air temperatures separated into different hours of day for **A** HW18, **B** HW19.1, and **C** HW19.2. The box shows the interquartile range (IQR) with the 25$^{th}$ (bottom) and 75$^{th}$ (top) percentile. The black line in the box shows the median. The vertical lines refer to the minimum (bottom) and maximum (top) value of the data within ± 1.5*IQR. Black dots denote outliers. The Taylor diagram in **D** shows hourly air temperature at 3 m above ground for all available loggers separated into six groups of four hours each. HW18 is shown as dots, HW19.1 as triangles, and HW19.2 as rectangles. The Pearson correlation coefficient is related to the azimuthal angle, the RMSE is proportional to the distance from the black circle on the x-axis, and the standard deviation is proportional to the radial distance from the origin and labelled on the x-axis.

**Tab. 5.** Adjusted $\mathbf{R^2_x}$ measure for the linear regression model fit of all the modelled and measured air temperatures at all available locations for 10:00, 14:00, 18:00, 22:00, 02:00, and 06:00 CEST, respectively. $\mathbf{df_x}$ shows the degrees of freedom for all chosen times of day

| | $R^2_{10}$ | $R^2_{14}$ | $R^2_{18}$ | $R^2_{22}$ | $R^2_{02}$ | $R^2_{06}$ | $df_{10}$ | $df_{14}$ | $df_{18}$ | $df_{22}$ | $df_{02}$ | $df_{06}$ |
|---|---|---|---|---|---|---|---|---|---|---|---|---|
| **HW18** | 0.18 | 0.42 | 0.28 | 0.43 | 0.11 | 0.30 | 600 | 597 | 373 | 375 | 375 | 375 |
| **HW19.1** | 0.11 | 0.18 | 0.10 | 0.09 | 0.14 | 0.07 | 598 | 598 | 523 | 523 | 448 | 448 |
| **HW19.2** | 0.17 | 0.75 | 0.47 | 0.32 | 0.30 | 0.10 | 288 | 287 | 295 | 295 | 221 | 221 |

The daily maximum (minimum) air temperatures are systematically lower (higher) than the measured air temperatures (Fig. 9). The modelled average daily air temperature range of minimum and maximum values per heat wave is 15.4 to 33.7 °C, 14.2 to 35.2 °C, and 15.0 to 32.9 °C during HW18, HW19.1, and HW19.2, respectively. The measured average daily air temperature range is 15.1 to 36.3 °C, 13.3 to 38.6 °C, and 15.7 to 38.6 °C during HW18, HW19.1, and HW19.2, respectively. HW19.1 shows the largest spread with both the lowest

measured average daily minimum air temperature and the highest measured average daily maximum air temperature of all the heat waves studied here. This is also modelled by MUKLIMO_3, but not to a sufficient extent, which leads to individual air temperatures biases of up to 10.9 K (Fig. 9B). HW18 and HW19.2 have a similar pattern, with MUKLIMO_3 underestimating the higher measured air temperatures in HW19.2 slightly more compared to HW18. Across all heat waves, the lowest modelled air temperatures are recorded between 06:00 and 09:00 CEST, whereas these are often already measured between 02:00 and 05:00 CEST, especially in HW19.1. The nocturnal cooling in the model thus takes place at a slower rate but reaches air temperatures similar to those measured by sunrise.

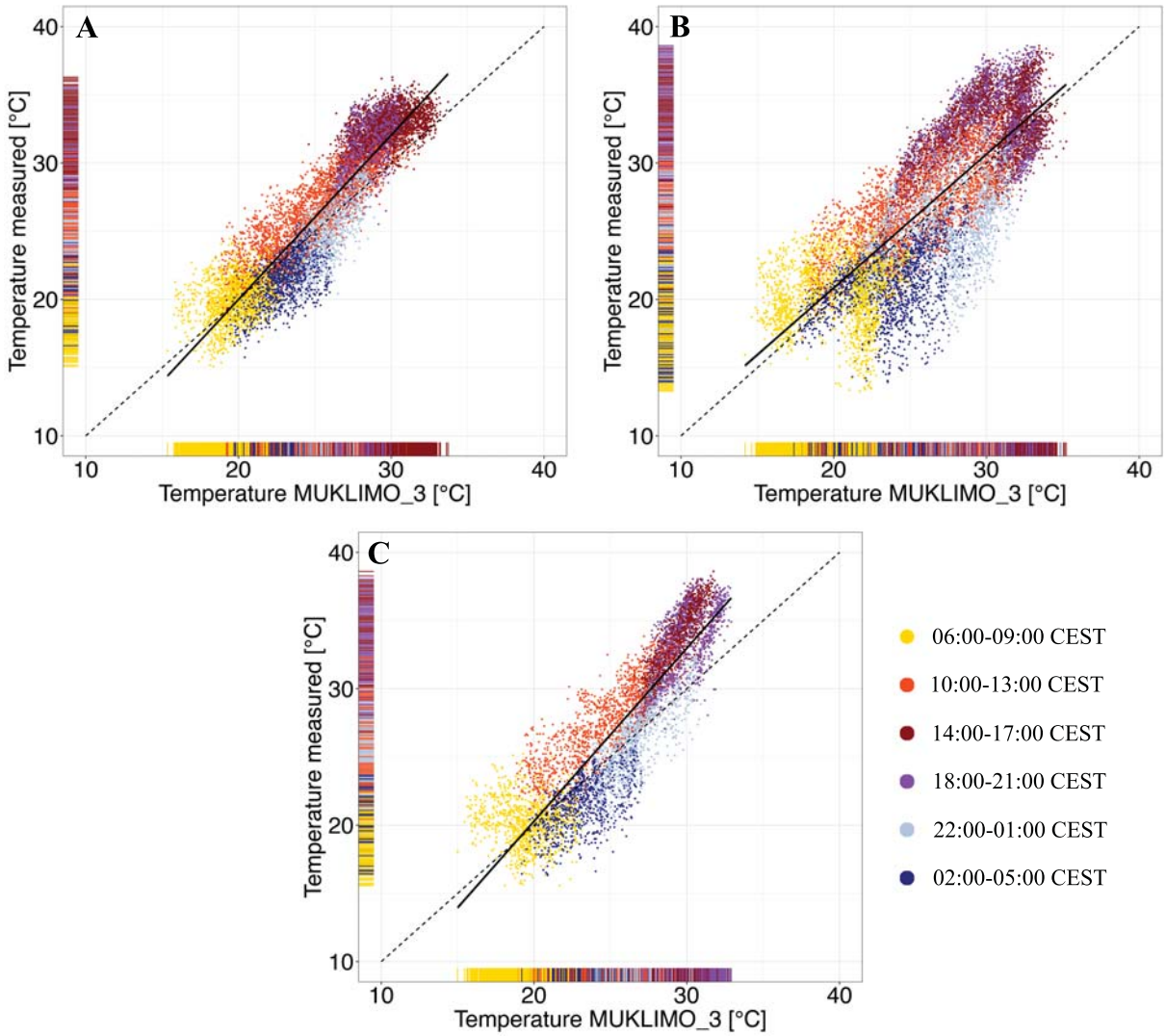


**Fig. 9.** Scatterplots of hourly air temperature of MUKLIMO_3 (x-axis) at 3 m above ground and measured air temperatures (y-axis) for **A** HW18, **B** HW19.1, and **C** HW19.2. The coloured bars on the axes represent the distribution of modelled and measured air temperatures, respectively. The dashed black line corresponds to slope 1, the solid black line corresponds to the linear regression.

## 3.2. Spatial evaluation

The hourly outputs of the air temperature fields at 3 m above ground from MUKLIMO_3 were spatially compared with the low-cost measurement network of Gubler et al. (2021) over the entire diurnal cycle, including all hours of day, separated into the respective heat wave. The comparison of all three heat waves has shown that the median air temperature 3 m above ground in MUKLIMO_3 is lower than the measured for all LCZs except for LCZ A in HW18 and HW19.1 and LCZ G in HW19.1 (Fig. 10A to C). In HW18, LCZ A shows the lowest (0.3 K) and LCZ E the highest absolute median bias (-1.6 K). In HW19.1, LCZ 8 shows the lowest (-0.3 K) and LCZ 10 the highest absolute median bias (-2.1 K). In HW19.2, LCZ A shows the lowest (-0.9 K) and LCZ 10 the highest absolute median bias (-3.3 K). HW19.1 shows a substantially higher variability and spread compared to HW18 and HW19.2. This also results in HW19.1 having a lower Pearson correlation of 0.79 and a RMSE of 3.4 K compared to HW18 and HW19.2 at 0.9 and 2.0 K over all LCZs, respectively (Fig. 10D). The standard deviation is similar in all heat waves under investigation. In general, it can be stated that built-up LCZs (LCZ 1 to 10) have similar median biases, higher Pearson correlations, higher standard deviations and lower RMSEs compared to land covered LCZs (LCZ A to G).

HW18 and HW19.2 show a good linear model fit with adjusted $R^2$ values of 0.79 to 0.90 and 0.71 to 0.88, respectively, with HW19.1 being lower at 0.55 to 0.67 for different LCZs over the entire diurnal cycle (Tab. 6). Across all heat waves, LCZ G shows the lowest and LCZ 1 the highest adjusted $R^2$ value. Built-up areas (LCZ 1 to 10) as well as LCZ A have higher adjusted $R^2$ values than the remaining land covered LCZs (LCZ B to G).

**Tab. 6.** Model performance of MUKLIMO_3 of different LCZs for all three heat waves. Adjusted $\mathbf{R^2_x}$ measure show the linear regression model fit of all the modelled and measured air temperatures 3 m above ground at all available time steps for LCZ 1, 2, 4, 5, 6, 8, 9, 10, A, B, D, E, and G, respectively. $\mathbf{df_x}$ shows the degrees of freedom for all LCZs

| | $R^2_1$ | $R^2_2$ | $R^2_4$ | $R^2_5$ | $R^2_6$ | $R^2_8$ | $R^2_9$ | $R^2_{10}$ | $R^2_A$ | $R^2_B$ | $R^2_D$ | $R^2_E$ | $R^2_G$ |
|---|---|---|---|---|---|---|---|---|---|---|---|---|---|
| **HW18** | 0.90 | 0.86 | 0.86 | 0.85 | 0.85 | 0.84 | 0.79 | - | 0.87 | 0.82 | 0.83 | 0.84 | 0.79 |
| **HW19.1** | 0.67 | 0.67 | 0.64 | 0.65 | 0.64 | 0.65 | 0.59 | 0.64 | 0.65 | 0.60 | 0.55 | 0.58 | 0.55 |
| **HW19.2** | 0.88 | 0.82 | 0.82 | 0.83 | 0.81 | 0.80 | 0.76 | 0.84 | 0.84 | 0.79 | 0.76 | 0.76 | 0.71 |
| | $df_1$ | $df_2$ | $df_4$ | $df_5$ | $df_6$ | $df_8$ | $df_9$ | $df_{10}$ | $df_A$ | $df_B$ | $df_D$ | $df_E$ | $df_G$ |
| **HW18** | 141 | 2308 | 432 | 2513 | 2168 | 433 | 142 | - | 431 | 865 | 433 | 578 | 432 |
| **HW19.1** | 334 | 3022 | 334 | 2350 | 2350 | 334 | 166 | 166 | 670 | 838 | 1006 | 502 | 502 |
| **HW19.2** | 85 | 1621 | 172 | 1216 | 1218 | 149 | 85 | 85 | 346 | 433 | 520 | 260 | 259 |

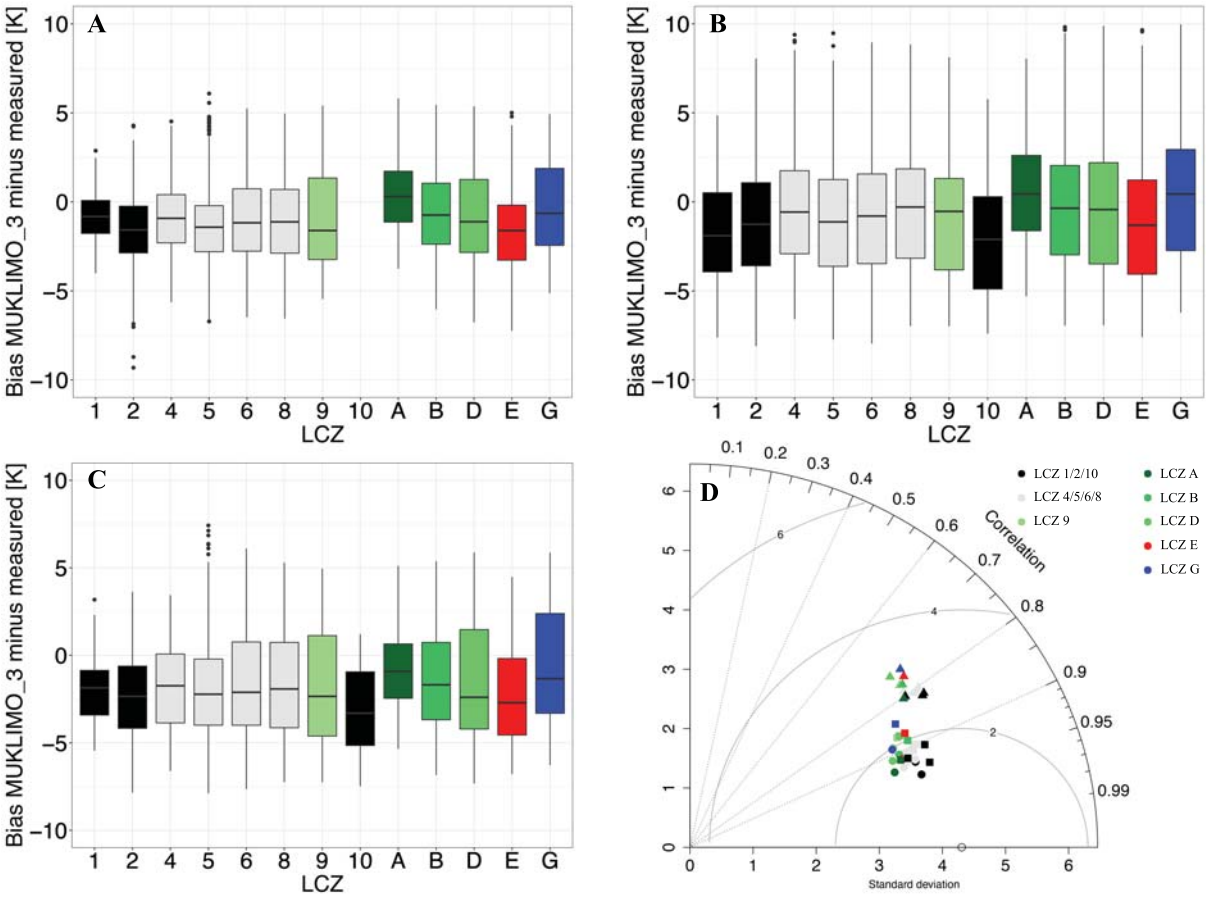


**Fig. 10.** Boxplots of hourly air temperature difference of MUKLIMO_3 at 3 m above ground and the measured air temperatures separated into different LCZ for **A** HW18, **B** HW19.1, and **C** HW19.2. The box shows the interquartile range (IQR) with the 25$^{th}$ (bottom) and 75$^{th}$ (top) percentile. The black line in the box shows the median. The vertical lines refer to the minimum (bottom) and maximum (top) value of the data within ± 1.5*IQR. The black dots denote outliers. The Taylor diagram in **D** shows hourly air temperature at 3 m above ground over the entire diurnal cycle separated into LCZs. HW18 is shown as dots, HW19.1 as triangles, and HW19.2 as rectangles. The Pearson correlation coefficient is related to the azimuthal angle, the RMSE is proportional to the distance from the black circle on the x-axis, and the standard deviation is proportional to the radial distance from the origin and labelled on the x-axis.

## 3.3. Evaluation of the urban heat island

The basic spatial pattern of UHI is similar between the heat waves investigated for each of the six time steps examined in MUKLIMO_3. At 10:00 CEST, mainly lower-lying areas without forest cover are affected by higher air temperatures of up to 1.8 K compared to Bern/Zollikofen (Fig. 11). Higher areas surrounding Bern and forests show air temperatures up to 2.9 K lower than Bern/Zollikofen. During the warming until the early afternoon, the area of increased air temperatures at 14:00 CEST is mainly concentrated in the built-up areas and accentuated at the same time to up to 2.7 K higher air temperatures than Bern/Zollikofen. While the urban forests lose some of their cooling effect and are only slightly cooler or in part already warmer than Bern/Zollikofen, the elevations in the surrounding countryside remain up to 4.4 K cooler than Bern/Zollikofen. Especially during HW18, lower-lying forest areas are warmer than

Bern/Zollikofen at 14:00 CEST. Until the early evening at 18:00 CEST the area of increased air temperatures is concentrated even more strongly on the built-up areas, but at the same time the difference in air temperature to Bern/Zollikofen decreases slightly to 2 K (Fig. 12). The forested areas are again slightly cooler than Bern/Zollikofen in all heat waves studied. The air temperature difference of the surrounding elevations to Bern/Zollikofen remains about the same at 4.2 K. Along the course of the river Aare, air temperatures are slightly lower than in the area directly next to it, although the cooling effect is not sufficient to achieve lower air temperatures than in Bern/Zollikofen, especially in the densely built-up inner city. With sunset, the situation changes at 22:00 CEST, with the area of increased air temperatures becoming substantially larger and also affecting unbuilt areas of the near vicinity of the city. The air temperature differences to Bern/Zollikofen are with up to 1.8 K in the same range as already at 18:00 CEST. In particular smaller forests no longer show any cooling effect. Larger forest areas, however, have the opposite effect and exhibit substantially cooler air temperatures than Bern/Zollikofen, to a similar extent as the surrounding elevations with up to 2.3 K. Higher air temperatures can also be seen in slightly elevated areas. At 22:00 CEST, the Aare shows a cooling effect only north and south of the city centre. In the first valleys, e.g. in the south of the model area, the air temperature on the valley floor begins to cool more strongly compared to higher elevated areas, which is the first sign of cold air drainage. At 02:00 CEST the area with increased air temperatures of up to 1.6 K higher than Bern/Zollikofen expands further and leads to even larger forested and higher elevated areas being only slightly cooler and in part already warmer than Bern/Zollikofen (Fig. 13). Further cold air drainages form in valleys in the east of the model area and existing ones intensify. These have air temperatures up to 2.5 K lower than Bern/Zollikofen. In the morning at 06:00 CEST, shortly before sunrise, the area of higher air temperatures is present far beyond the city boundaries, especially towards the southeast. The water of the Aare has higher temperatures than the surrounding air, so that the river exerts a warming effect on the nearby surroundings. The slopes of the elevations in the south and east show higher air temperatures than Bern/Zollikofen in many places at up to 300 m above the city area. This effect is less pronounced in HW18 than in HW19.1 and HW19.2. In all heat waves, air temperatures are up to 1.8 K higher than in Bern/Zollikofen at 06:00 CEST, especially along the Aare.

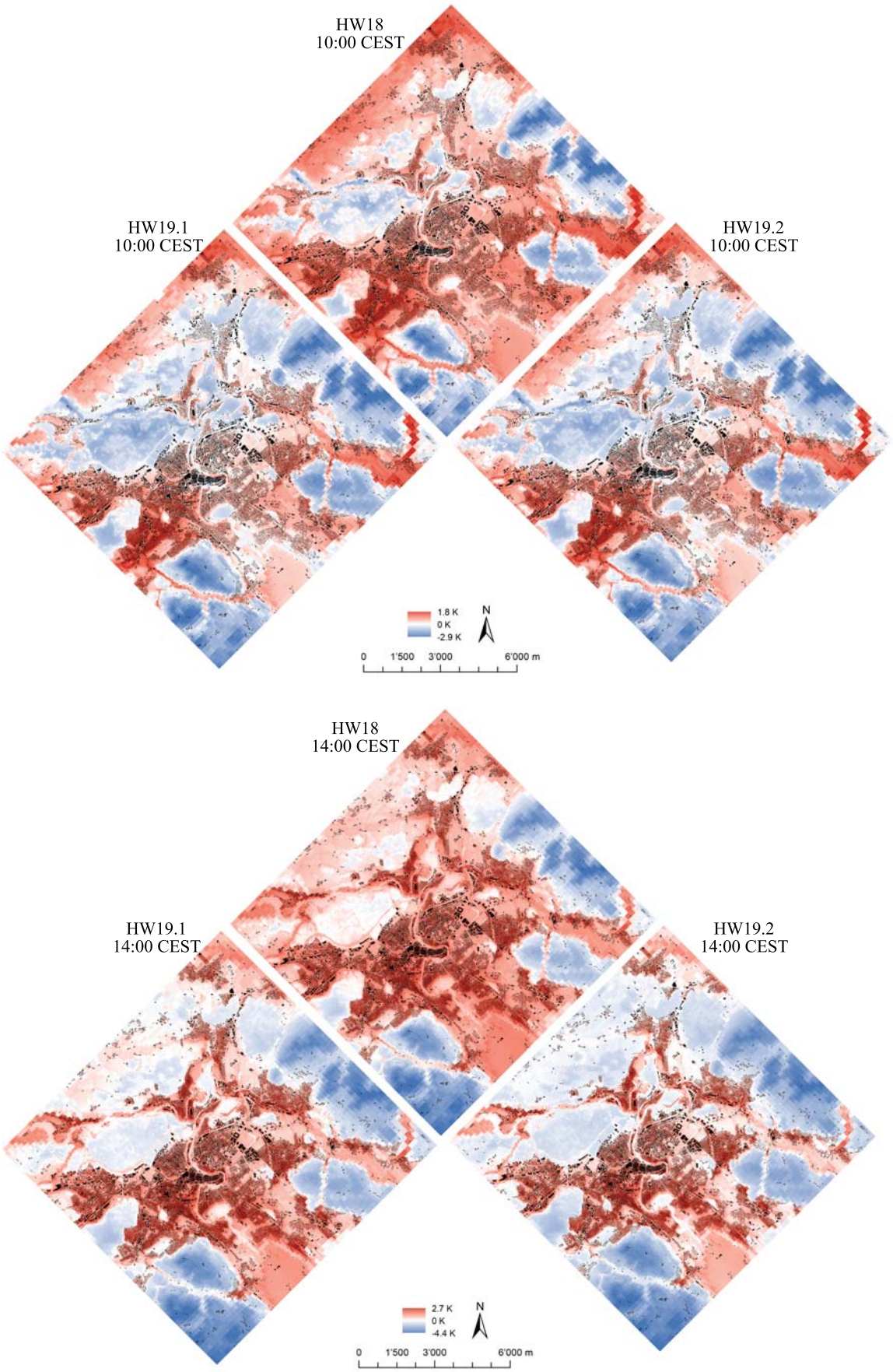


**Fig. 11.** Maps of UHI showing the difference of the mean air temperature of MUKLIMO_3 of each grid cell compared to the grid cell of the measurement site Bern/Zollikofen for 10:00 and 14:00 CEST for each individual heat wave. In black are all the buildings (swisstopo, 2021).

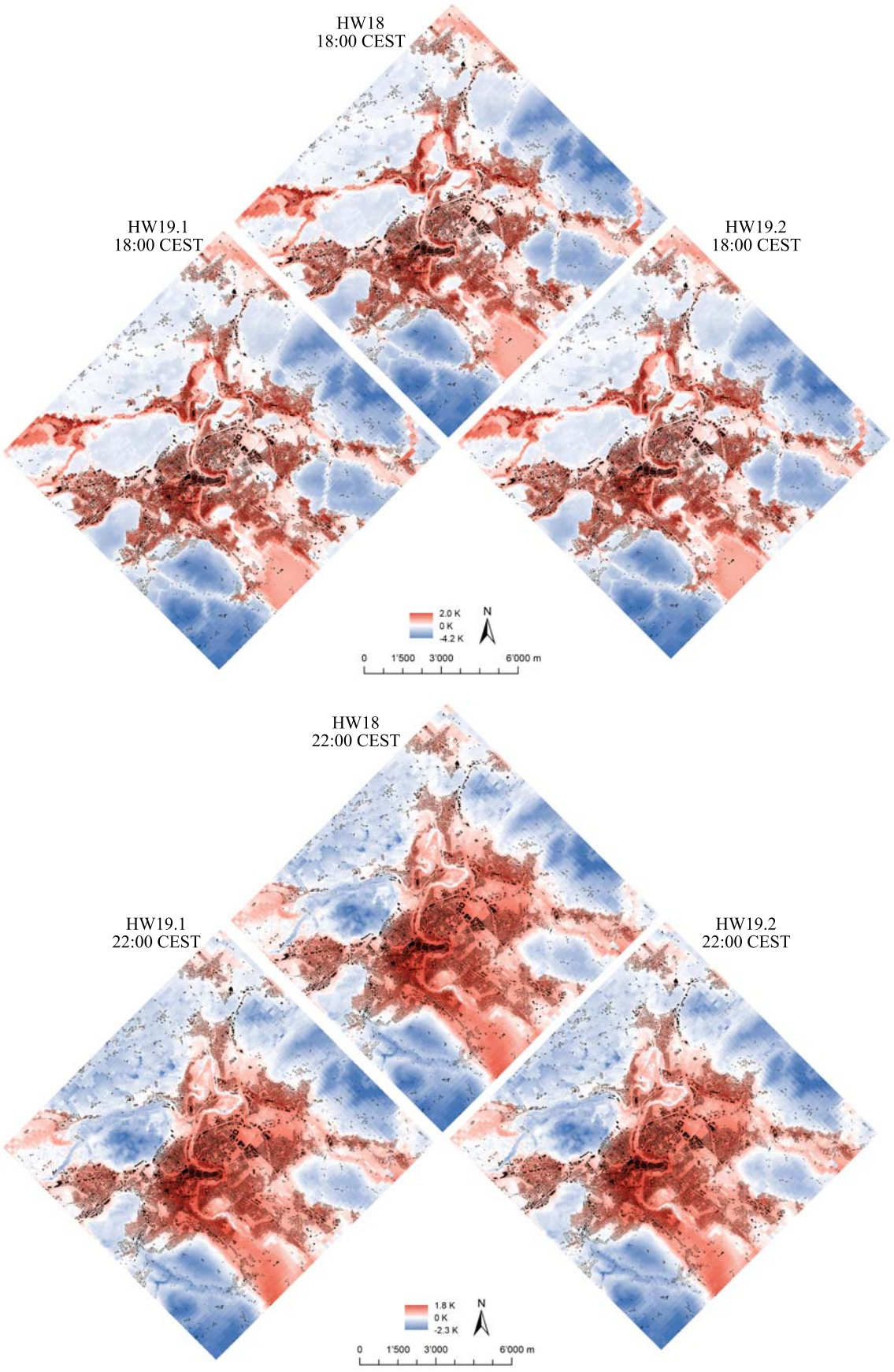


**Fig. 12.** Maps of UHI showing the difference of the mean air temperature of MUKLIMO_3 of each grid cell compared to the grid cell of the measurement site Bern/Zollikofen for 18:00 and 22:00 CEST for each individual heat wave. In black are all the buildings (swisstopo, 2021).

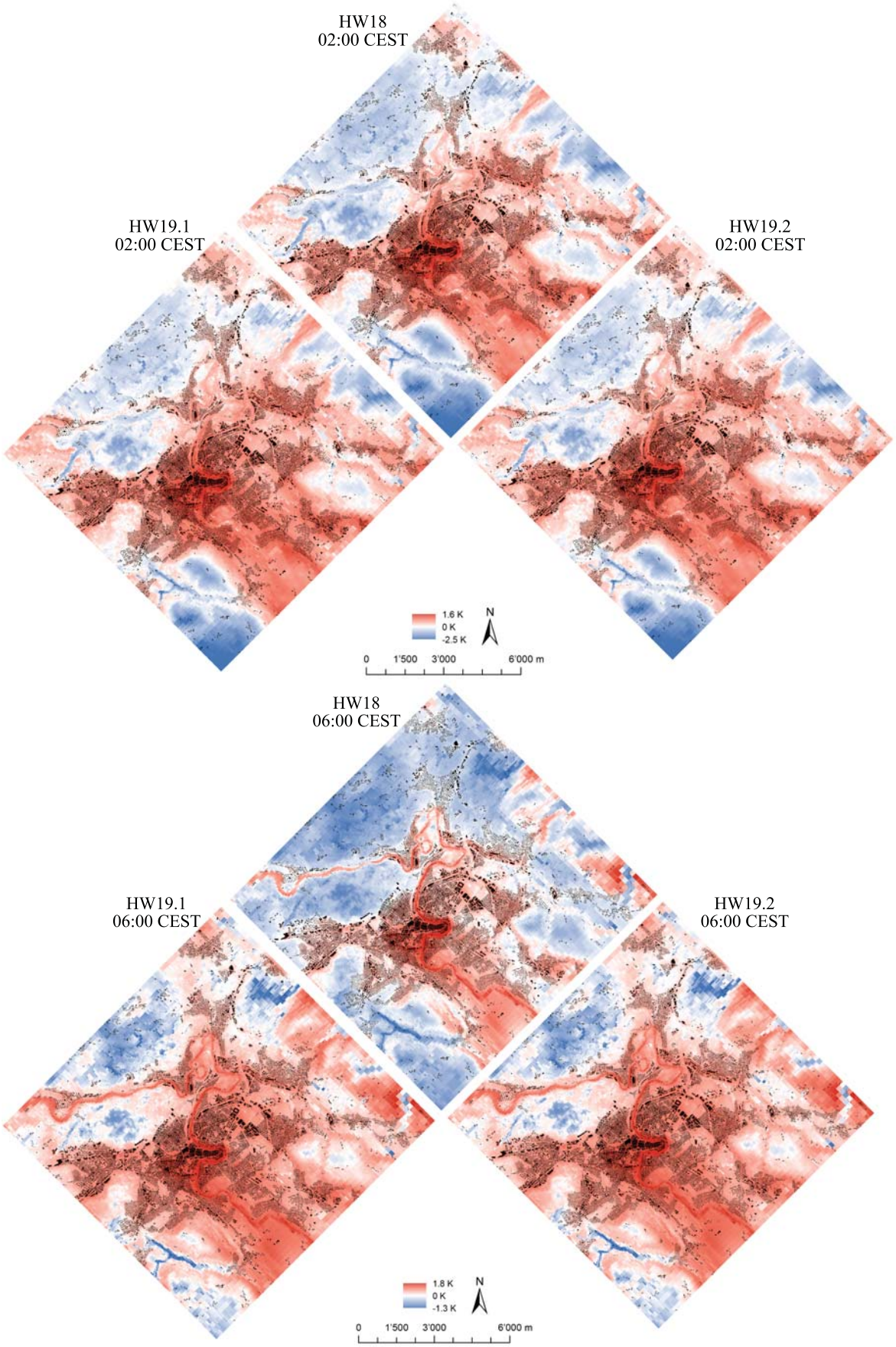


**Fig. 13.** Maps of UHI showing the difference of the mean air temperature of MUKLIMO_3 of each grid cell compared to the grid cell of the measurement site Bern/Zollikofen for 02:00 and 06:00 CEST for each individual heat wave. In black are all the buildings from (swisstopo, 2021).

# 4. Discussion

It was shown that MUKLIMO_3 could model the basic spatiotemporal air temperature distribution patterns in the area of Bern during rainless days in heat waves by heating up in particular the densely built-up inner city during the day and forming a large-scale UHI at night, which is also partly influenced by cold air drainages. However, the differences between MUKLIMO_3 and the air temperature measurements as well as the different performance of the modelling in the individual heat waves require a discussion of possible influencing factors, which can be found in the meteorological conditions, the modelling itself as well as the measurements.

## 4.1. Meteorological conditions

While HW18 at Bern/Zollikofen and Bantiger were mainly dominated by the wind direction northeast during the entire diurnal cycle, HW19.2 experienced a stronger influence of south-westerly winds from 02:00 to 09:00 CEST. HW19.1 had noticeable amounts of wind from the south to southwest already from 22:00 to 09:00 CEST. The change in wind direction from 22:00 CEST in HW19.1 occurred during the time when MUKLIMO_3 had the largest positive deviations from the measurements, as well as the highest RMSE and lowest Pearson correlations (Fig. 8B/D). The poorer statistical values can be explained by cold air advections, which occurred more frequently in HW19.1 compared to HW18 and HW19.2. From 27 June 2019, colder air flowed in from the north towards Switzerland on high altitude in the evening, which could be measured at the Jungfraujoch station (3582 m a.s.l.) with a decrease of air temperature of 7 K within 48 hours (MeteoSwiss, 2021). While the first three nights of HW19.1 from 24 to 26 June 2019 showed hardly any difference between modelled and measured air temperature, this rose to over 7 K in the subsequent nights of 27 to 29 June 2019 (see Appendix Fig. A1). Another possible explanation for colder nights during HW19.1 in Bern is alpine pumping, which is a regional circulation phenomenon that occurs during the day between the Alps and the lowlands when there is strong solar radiation and a weak pressure gradient, as it is the case during heat waves (Winkler et al., 2006). During the night, the cold air forming along the Alps flows out and advances through the Aare valley to Bern. These two types of mesoscale cold air advection cannot be detected by MUKLIMO_3, which likely resulted in an overestimation of the air temperature. Especially during HW19.1 there were more winds from different directions in Bern/Zollikofen and Bantiger, and therefore potentially more mesoscale

influences on the air temperature field in the area of Bern. To overcome this problem, a link to regional and global models would be necessary, as it is the case for WRF with nested domains for urban applications (Holec et al., 2020). Hollósi et al. (2021) has coupled MUKLIMO_3 with a numerical weather prediction model, but this did not improve the day-to-day intra-urban variations in microclimate compared to real atmospheric conditions as input variables.

Another meteorologically induced uncertainty is the soil moisture, which is indicated in MUKLIMO_3 via classes from 1 (very dry) to 6 (very moist). Since the model tends to overestimate evapotranspiration, small values of 1 to 2 are recommended (DWD, 2020). If rain fell on the previous day, a value of 2 was used, otherwise 1. However, since the rain did not fall uniformly over the entire model area and the soil was likely able to absorb different amounts of water depending on the previous dryness, the real soil moisture is difficult to estimate and is subject to some uncertainties.

The soil temperature must be given to the model at a depth of 1 m (DWD, 2020). This parameter is then used over the entire model area, apart from the water areas, and adjusted according to altitude and tree cover. However, measured values are only available up to a depth of 0.5 m in Bern/Zollikofen, so that a greater depth must be estimated and is correspondingly uncertain. In order to estimate the soil temperatures at a depth of 1 m, these were compared at a depth of 0.5 m in Bern/Zollikofen with those in Singen (Germany), at a distance of 140 km and at a similar altitude to Bern/Zollikofen, where the measurements are done at a depth of 0.5 m and 1 m. This allowed the temperature difference between 0.5 m and 1 m in Singen to be applied to Bern/Zollikofen. However, there are uncertainties in this calculation, so deviations in the actual soil temperature at 1 m depth are likely. Straka & Sodoudi (2019) could show that deviations in soil temperature can lead to considerable changes in the output of MUKLIMO_3, so temperature measurements at a depth of 1 m would be important for improving the modelling.

## 4.2. Inaccuracies of MUKLIMO_3

The differences between measured and modelled air temperatures during the day are most likely due to different phenomena. While the too low modelled air temperatures during the day are likely due to measurements error (see Section 4.3), the deviations at night are rather because of MUKLIMO_3, in that the cooling after sunset was modelled too slowly (Elzafarany et al., 2017; Geletič et al., 2016; Kielar et al., 2017; Straka & Sodoudi, 2019). This also tends to lead

to higher RMSE at night. As a result, high amount of outgoing radiation can take place at night. In the model, the cloud cover is fixed over the entire model run, so that the outgoing radiation at night was presumably modelled too weakly.

MUKLIMO_3 simulates a substantially smaller UHI than that measured by the air temperature measurement network. A possible factor can be found in the spatial extent of the UHI, which extends very far at night, especially to the north and southeast (Fig. 13). The rural measurement site Bern/Zollikofen seems to be under urban air temperature influence at night in MUKLIMO_3, especially in HW19.1 and HW19.2, so that rural air temperatures independent of the city are no longer reflected there, but higher ones caused by the UHI. A probable explanation for this phenomenon can be found in the more frequent wind from the south to southeast, which occurred mainly in these two heat waves. This creates a plume from the city towards the north to north-east, which thus also influences the air temperatures in Bern/Zollikofen and thus reduces the air temperatures difference between Bern/Zollikofen and the urban areas in the city centre. A proposed solution to this problem is to set up a more distant measurement site outside this plume or to use several rural measurement sites at different directions from the city centre, whose air temperatures could be averaged and thus reduce the influence of individual plumes.

Even within the city, the modelled air temperature differences between the individual LCZs are smaller than the measured ones. This might be due to the horizontal spatial resolution per grid cell of 50 x 50 m, which means that small-scale air temperature fluctuations are lost and thus, for example, high nocturnal air temperatures in the city centre can only be captured inadequately. It is also likely due to the unresolved buildings, which leads to further inaccuracies. Resolved buildings are not considered by the model and instead they are divided into five different categories of grid cells that contain buildings to a different proportion. MUKLIMO_3 forms an ensemble for each grid cell with different realisations of the unresolved buildings, so that the arrangement of the buildings is different, but the proportion of buildings is constant. An average value for all meteorological parameters is then calculated from this ensemble (Sievers, 2016). Furthermore, a simplification in MUKLIMO_3 leads to further uncertainties at grid cell level, in that individual grid cells may only contain buildings or trees, but not both together. However, tree vegetation in built-up areas can play an important role for the air temperature (Scott et al., 1999). Neighbourhoods with relatively extensive tree cover can therefore not be adequately modelled, as the tree cover must be ignored if the building areas dominate. Moreover, all parameters defining the properties of a grid cell are determined for a cell size of 50 x 50 m and adopted for all other grid cell sizes in the nesting.

Especially for the larger grid cells at the boundaries of the model area, these parameters could be defined separately and thus the accuracy of the input factors could be increased by additional LUCs. Furthermore, since the version of MUKLIMO_3 used in this study, instead of a land use table, a raster data set of parameters can also be used, so that each grid cell can have different parameter values (DWD, 2020).

The vertical temperature field is determined by interpolation based on air temperature measurements in Bern/Zollikofen and Bantiger. Yet this could only inadequately represent the vertical temperature distribution in the atmosphere, especially in the case of a non-adiabatic air temperature distribution, as occurs on nights with strong radiative emission and a developing air temperature inversion forming (Godowitch et al., 1985). In MUKLIMO_3, air temperatures can be specified at up to five different altitudes, so that an interpolation between different altitudes would have to be carried out by the model with less vertical distance and would therefore also be less prone to errors (DWD, 2020).

The wind field is not only an uncertainty factor due to possible cold air advections, but also due to its definition in MUKLIMO_3. It's determined on an hourly basis at a fixed altitude of 826 m a.s.l. in the middle between Bern/Zollikofen (555 m a.s.l.) and Bantiger (1097 m a.s.l.) as the mean wind speed and direction and is determined internally by the model for all other altitudes. Due to the complex topography in Bern, the two measurement sites may not reflect the wind field over the entire model area. Furthermore, abrupt changes in wind speed or direction from one hour to the next can lead to numerical instabilities, which cause the model run the be aborted. Therefore, the wind field must be smoothed by adjusting certain hourly wind speeds and directions to avoid large changes in the wind field of successive hourly values. Since the wind field has changed considerably, especially shortly before thunderstorms, 3 % of all wind speeds and directions had to be changed in HW18, 6 % in HW19.1, and 5 % in HW19.2.

In contrast to the wind field, which is given to MUKLIMO_3 hourly, all other meteorological input factors are fixed at the start of the respective model run. Therefore, the conditions at 07:00 CEST have a great influence on the further course of the modelling. If, for example, the cloud cover changes significantly during a model run, this leads to a change in both solar irradiation and emissivity, to a change in evaporation and to a change in the wind field within the city. However, this is not captured by MUKLIMO_3. Hollósi et al. (2021) mention that a positive or negative cloud cover bias highly influences the diurnal ranges of temperature and relative humidity and could show that excluding simulations of cloud cover bias of more than 50 % improve the air temperature results by about 10 %.

Along the upper and lateral model boundaries, the 1D model of MUKLIMO_3 provides values for the 3D model (see Section 2.8). In case of complex topography with relatively steep slopes of the terrain surface along the model boundaries, winds from the 3D model can conflict with winds from the 1D model and lead to numerical instabilities (Sievers, 2012, 2016). This is the case in Bern, where the lateral model boundaries extend along hills in both the south and the east. As a solution to this problem, additional grid cells are artificially added along the model boundaries that do not have a slope (DWD, 2020). However, this does not correspond to reality and is a possible explanation for the occasionally conspicuously high air temperatures along the north-eastern model boundary. Increasing the size of the model area in the horizontal direction would help to minimise the problems along the lateral model boundaries by removing these areas from further analysis.

## 4.3. Inaccuracies of the measurements

Compared to official air temperature measurements by MeteoSwiss and the city's office for environmental protection, the air temperature measurements of the high-resolution air temperature measurement network take place only passively ventilated. Gubler et al. (2021) could detect air temperature deviations of typically 0.78-1.17 K, but up to 2 K and more during heat waves at daytime in HW18 compared to actively ventilated air temperature measurements at the reference stations (see Fig. 7). The underestimation of the modelled air temperatures at the hottest time of the day of 3-4 K over all heat waves investigated can thus be explained to a large extent by an overestimation of the measured air temperatures. Measurement sites in the inner city, which are affected by less wind due to the increased surface roughness caused by the surrounding buildings and at the same level of solar irradiation, the passive ventilation is less efficient, so that the error is additionally increased. Shaded sites, which are less affected by air temperature measurement errors due to solar irradiance, such as forests in LCZ A, show a lower deviation than all other LCZs.

# 5. Conclusion

The aim of this study was to model the spatial and temporal air temperature distribution on an hourly basis for the greater area of Bern during the three distinct heat waves HW18, HW19.1, and HW19.2 and to validate the model performance with the high-resolution temperature measurement network of Gubler et al. (2021).

It could be shown that MUKLIMO_3 is able to realistically represent the spatiotemporal air temperature distribution in the greater area of Bern for rainless days during heat waves. Especially on calm, radiation-intensive days without thunderstorm formation and mesoscale cold air advection, the modelled air temperature showed a high degree of agreement with the measured values. This was the case almost equally across all LCZs. During the day, the maximum air temperatures were underestimated, and the nocturnal air temperatures were overestimated compared to the measured air temperatures, especially in the first half of the night. However, the lowest air temperatures in the early morning showed only a slight bias to the measured air temperatures. In general, MUKLIMO_3 was best able to model the highest air temperatures in the afternoon, as up to 75 % of the variance (HW19.2 at 14:00 CEST) in the air temperature difference to the measured values could be explained (adjusted $R^2$: 0.75), which was also noted by Hollósi et al. (2021). At the same time, the model also showed the highest deviations from the measured air temperature, which can partly be explained by the bias of the air temperature measurements.

HW19.1 performs worse than the other two heat waves in various aspects: a worse Pearson correlation, a higher RMSE, a larger median bias over the course of the day and a larger spread of air temperature deviations. HW19.1 showed a similar air temperature distribution as HW18 and HW19.2 for all hours investigated during the course of the day, which is why the poorer performance of HW19.1 can be explained by phenomena not integrated in the model, such as cold air advections.

The study demonstrated the potential of using MUKLIMO_3 to obtain the spatiotemporal air temperature distribution during heat waves. Areas with increased air temperatures and thus greater heat stress during the day as well as at night can be identified and provide important indications for future urban development measures. In particular, days without cold air advection or precipitation and with little wind, which generally lead to the greatest heat load in heat waves, can be modelled realistically with MUKLIMO_3. Furthermore, MUKLIMO_3 makes it possible to model major urban development measures such as new neighbourhoods or new urban parks to estimate their effect on air temperature. However, small-scale measures

such as additional trees along streets and squares cannot be modelled realistically due to limitations in the model and its setup.

## Acknowledgments

I would like to thank my supervisor Prof. Dr. Stefan Brönnimann and my two advisors Dr. Moritz Gubler and Moritz Burger for their patience and their numerous and valuable inputs during the whole process of my master thesis. Furthermore, I would like to thank the entire urban climate group, Saba, and Lukas in addition to those already mentioned, for implementing and operating the air temperature measurement network, without which a study in the presented form would not have been possible. Another big thank you goes to Brigitta Hollósi from the Central Institute for Meteorology and Geodynamics in Vienna, Austria. Especially during the implementation phase of the MUKLIMO_3 simulations, she was an important support and answered my open questions in a detailed way in numerous emails and zoom meetings. I would also like to thank Heike Schau-Noppel and Saskia Buchholz from the German Weather Service. They supported me in particular with detailed technical questions about MUKLIMO_3 and made a decisive contribution to ensuring that the simulations ran error-free as quickly as possible. Last but not least, I would like to thank Sandro for his patience during the long time at home in the home office and for proofreading the thesis.

## References

Amt für Geoinformation des Kantons Bern. (2021). *Amtliche Vermessung vereinfacht*. https://www.geo.apps.be.ch/de/geodaten/geoprodukte-zum-download-1/sheet/de-DE/a71ad9ac-4e0f-cac4-816b-a0bd22237c16/dlgeoproducts/complete/search_list.html

Baccini, M., Biggeri, A., Accetta, G., Kosatsky, T., Katsouyanni, K., Analitis, A., Anderson, H. R., Bisanti, L., D'Iippoliti, D., Danova, J., Forsberg, B., Medina, S., Paldy, A., Rabczenko, D., Schindler, C., & Michelozzi, P. (2008). Heat effects on mortality in 15 European cities. *Epidemiology*, *19*(5), 711–719. https://doi.org/10.1097/EDE.0b013e318176bfcd

BFS, & Schweizerischer Städteverband. (2020). *Statistik der Schweizer Städte 2020*. https://www.bfs.admin.ch/bfs/de/home/statistiken/kataloge-datenbanken/publikationen.assetdetail.12767482.html

Bundesamt für Umwelt. (2019). Hitze und Trockenheit im Sommer 2018 - Auswirkungen auf Mensch und Umwelt. *Umwelt-Zustand*, *1909*, 91.

DWD. (2020). *User's Guide MUKLIMO_3 Thermodynamic v200629*.

Elzafarany, A., Abouelseoud, T., Ashraf, H., & Sodoudi, S. (2017). Estimate of climate change impacts on urban heat island using an urban climate modelling in Desert City case study,"Greater Cairo" Egypt. *1st MUKLIMO_3 Users Workshop May. 2017*.

European Environment Agency. (2020a). *Imperviousness Density 2018*. https://land.copernicus.eu/pan-european/high-resolution-layers/imperviousness/status-maps/imperviousness-density-2018?tab=mapview

European Environment Agency. (2020b). *Tree Cover Density*. https://land.copernicus.eu/pan-european/high-resolution-layers/forests/tree-cover-density/status-maps/tree-cover-density-2018?tab=mapview

Federal Office for the Environment. (2021). *Hydrological Data*. https://www.hydrodaten.admin.ch/en/2135.html

Feranec, J., Holec, J., Šťastný, P., Szatmári, D., & Kopecká, M. (2019). Visualising a comparison of simulated urban heat islands: a case study of two Slovakian cities. *Advances in Cartography and GIScience of the ICA*, *1*, 1–8. https://doi.org/10.5194/ica-adv-1-6-2019

Fernandez Milan, B., & Creutzig, F. (2015). Reducing urban heat wave risk in the 21st century. *Current Opinion in Environmental Sustainability*, *14*, 221–231. https://doi.org/10.1016/j.cosust.2015.08.002

Geletič, J., Lehnert, M., & Dobrovolný, P. (2016). Modelled spatio-temporal variability of air temperature in an urban climate and its validation: A case study of Brno, Czech Republic. *Hungarian Geographical Bulletin*, *65*(2), 169–180. https://doi.org/10.15201/hungeobull.65.2.7

Geletič, J., Lehnert, M., Savić, S., & Milošević, D. (2018). Modelled spatiotemporal variability of outdoor thermal comfort in local climate zones of the city of Brno, Czech Republic. *Science of the Total Environment*, *624*, 385–395. https://doi.org/10.1016/j.scitotenv.2017.12.076

Ginzler, C., & Hobi, M. L. (2015). Countrywide stereo-image matching for updating digital surface models in the framework of the swiss national forest inventory. *Remote Sensing*, *7*(4), 4343–4370. https://doi.org/10.3390/rs70404343

Godowitch, J. M., Ching, J. K. S., & Clarke, J. F. (1985). Evolution of the Nocturnal Inversion Layer at an Urban and Nonurban Location. *Meteorology and Assessment*

*Division, Atmospheric Sciences Research Laboratory, Environmental Protection Agency, Research Trangle Park, NC 27711*, *24*(8), 791–804. https://doi.org/10.1175/1520-0450(1985)024<0791:EOTNIL>2.0.CO;2

Gross, G. (1989). Numerical simulations of the nocturnal flow systems in the Freiburg area for different topographies. *Beiträge Zur Physik Der Atmosphäre*, *62*, 57–72.

Gubler, M., Christen, A., Remund, J., & Brönnimann, S. (2021). Evaluation and application of a low-cost measurement network to study intra-urban temperature differences during summer 2018 in Bern, Switzerland. *Urban Climate*, *37*. https://doi.org/10.1016/j.uclim.2021.100817

Holec, J., Feranec, J., Šťastný, P., Szatmári, D., Kopecká, M., & Garaj, M. (2020). Evolution and assessment of urban heat island between the years 1998 and 2016: case study of the cities Bratislava and Trnava in western Slovakia. *Theoretical and Applied Climatology*, *141*(3–4), 979–997. https://doi.org/10.1007/s00704-020-03197-1

Hollósi, B., Žuvela-Aloise, M., Oswald, S., Kainz, A., & Schöner, W. (2021). Applying urban climate model in prediction mode—evaluation of MUKLIMO_3 model performance for Austrian cities based on the summer period of 2019. *Theoretical and Applied Climatology*, *144*(3–4), 1181–1204. https://doi.org/10.1007/s00704-021-03580-6

IPCC. (2014). Climate Change 2014: Synthesis Report. Contribution of Working Groups I, II and III to the Fifth Assessment Report of the Intergovernmental Panel on Climate Change [Core Writing Team, R.K. Pachauri and L.A. Meyer (eds.)]. *IPCC, Geneva, Switzerland, 151 Pp.*

Kachelmannwetter. (2021). *Regenradar und Schneeradar Schweiz*. https://kachelmannwetter.com/ch/regenradar/schweiz

Kielar, R., Ostapowicz, K., Bokwa, A., Buchholz, S., Noppel, H., Žuvela-Aloise, M., & Hollosi, B. (2017). MUKLIMO_3 results verification for Kraków, Poland. *1st MUKLIMO_3 Users Workshop May 9–10, 2017*.

Kleerekoper, L., Van Esch, M., & Salcedo, T. B. (2012). How to make a city climate-proof, addressing the urban heat island effect. *Resources, Conservation and Recycling*, *64*, 30–38. https://doi.org/10.1016/j.resconrec.2011.06.004

Kopecká, M., Szatmári, D., Holec, J., & Feranec, J. (2021). Urban heat island modelling based on MUKLIMO: examples from Slovakia. *AGILE: GIScience Series*, *2*, 1–11. https://doi.org/10.5194/agile-giss-2-5-2021

Kottek, M., Grieser, J., Beck, C., Rudolf, B., & Rubel, F. (2006). World map of the Köppen-

Geiger climate classification updated. *Meteorologische Zeitschrift*, *15*(3), 259–263. https://doi.org/10.1127/0941-2948/2006/0130

Kovats, R. S., & Kristie, L. E. (2006). Heatwaves and public health in Europe. *European Journal of Public Health*, *16*(6), 592–599. https://doi.org/10.1093/eurpub/ckl049

Le Tertre, A., Lefranc, A., Eilstein, D., Declercq, C., Medina, S., Blanchard, M., Chardon, B., Fabre, P., Filleul, L., Jusot, J. F., Pascal, L., Prouvost, H., Cassadou, S., & Ledrans, M. (2006). Impact of the 2003 heatwave on all-cause mortality in 9 French cities. *Epidemiology*, *17*(1), 75–79. https://doi.org/10.1097/01.ede.0000187650.36636.1f

Mathys, H., Maurer, R., Messerli, B., Wanner, H., & Winiger, M. (1980). Klima und Lufthygiene im Raum Bern. *Geographica Bernensia*, *G12*. https://boris.unibe.ch/130365/1/G12_low.pdf

Matsaba, E. O., Langer, I., Adimo, A. O., Mukundi, J. B., & Wesonga, J. M. (2020). Spatio-Temporal Variability of Simulated 2 m Air Temperature for Nairobi City, Kenya. *Current Urban Studies*, *08*(02), 205–221. https://doi.org/10.4236/cus.2020.82011

MeteoSwiss. (2018). Hitze und Trockenheit im Sommerhalbjahr 2018 - eine klimatologische Übersicht. *Fachbericht MeteoSchweiz*, *272*, 38.

MeteoSwiss. (2019). *Heat wave*. https://web.archive.org/web/20191115033924/https://www.meteoswiss.admin.ch/home/weather/gefahren/explanation-of-the-danger-levels/heat-wave.html

MeteoSwiss. (2020a). *Climate Normals Bern / Zollikofen*. https://www.meteoswiss.admin.ch/product/output/climate-data/climate-diagrams-normal-values-station-processing/BER/climsheet_BER_np8110_e.pdf

MeteoSwiss. (2020b). Klimareport 2019. *Bundesamt Für Meteorologie Und Klimatologie MeteoSchweiz*, 96.

MeteoSwiss. (2021). *IDAWEB*. https://gate.meteoswiss.ch/idaweb/login.do?language=en

Muthers, S., Laschewski, G., & Matzarakis, A. (2017). The summers 2003 and 2015 in South-West Germany: Heat waves and heat-related mortality in the context of climate change. *Atmosphere*, *8*(11). https://doi.org/10.3390/atmos8110224

Oke, T. R. (1973). City size and the urban heat island. *Atmospheric Environment (1967)*, *7*(8), 769–779. https://doi.org/10.1016/0004-6981(73)90140-6

Oke, T. R. (1995). The Heat Island of the Urban Boundary Layer: Characteristics, Causes and Effects. *Wind Climate in Cities*, 81–107. https://doi.org/10.1007/978-94-017-3686-2_5

Ragettli, M. S., & Röösli, M. (2020). Gesundheitliche Auswirkungen von Hitze in der Schweiz und die Bedeutung von Präventionsmassnahmen. *Schweizerisches Tropen- Und*

*Public Health-Institut*. https://www.nccs.admin.ch/dam/nccs/de/dokumente/website/sektoren/gesundheit/swisstph-2020-gesundheitliche-auswirkungen-von-hitze-2019-vergleich.pdf.download.pdf/SwissTPH_2020_Gesundheitliche Auswirkungen von Hitze_2019_Vergleich 2003-2015-2018_def.pdf

Rothfusz, L. P. (1990). The Heat Index "Equation" (or, More Than You Ever Wanted To Know About Heat Index). *Fort Worth, Texas: National Oceanic and Atmospheric Administration, National Weather Service, Office of Meteorology*. https://www.weather.gov/media/ffc/ta_htindx.PDF

Scott, K. I., Simpson, J. R., & McPherson, E. G. (1999). Effects of tree cover on parking lot microclimate and vehicle emissions. *Journal of Arboriculture*, *25*(3), 129–142. https://www.fs.usda.gov/treesearch/pubs/60567

Siebert, J., Sievers, U., & Zdunkowski, W. (1992). A one-dimensional simulation of the interaction between land surface processes and the atmosphere. *Boundary-Layer Meteorology*, *59*(1–2), 1–34. https://doi.org/10.1007/BF00120684

Sievers, U. (2012). Das kleinskalige Strömungsmodell MUKLIMO_3 Teil 1: Theoretische Grundlagen, PC-Basisversion und Validierung. *Selbstverlag Des Deutschen Wetterdienstes, Offenbach Am Main*. https://www.dwd.de/DE/leistungen/pbfb_verlag_berichte/l_einzelbaende/berichte240.html

Sievers, U. (2016). Das kleinskalige Strömungsmodell MUKLIMO_3 - Teil 2: Thermodynamische Erweiterungen. *Selbstverlag Des Deutschen Wetterdienstes, Offenbach Am Main*. https://www.dwd.de/DE/leistungen/pbfb_verlag_berichte/l_einzelbaende/berichte248.html

Sievers, U., Forkel, R., & Zdunkowski, W. (1983). Transport equations for heat and moisture in the soil and their application to boundary layer problems. *Beiträge Zur Physik Der Atmosphäre*, *56*, 58–83.

Sievers, U., & Zdunkowski, W. (1986). A microscale urban climate model. *Contrib. Atmos. Phys.*, *59*, 13–40.

Stewart, I. D., & Oke, T. R. (2012). Local climate zones for urban temperature studies. *Bulletin of the American Meteorological Society*, *93*(12), 1879–1900. https://doi.org/10.1175/BAMS-D-11-00019.1

Straka, M., & Sodoudi, S. (2019). Evaluating climate change adaptation strategies and

scenarios of enhanced vertical and horizontal compactness at urban scale (a case study for Berlin). *Landscape and Urban Planning*, *183*, 68–78. https://doi.org/10.1016/j.landurbplan.2018.11.006

swisstopo. (2018). *swissALTI3D*. https://www.swisstopo.admin.ch/en/geodata/height/alti3d.html

swisstopo. (2021). *swissBUILDINGS3D 2.0*. https://www.swisstopo.admin.ch/en/geodata/landscape/buildings3d2.html

Taylor, K. E. (2001). Summarizing multiple aspects of model performance in a single diagram. *Journal of Geophysical Research*, *106*(D7), 7183–7192. https://doi.org/10.1029/2000JD900719

United Nations, Department of Economic and Social Affairs, P. D. (2019). World Urbanization Prospects: The 2018 Revision (ST/ESA/SER.A/420). In *Demographic Research*. https://population.un.org/wup/Publications/Files/WUP2018-Report.pdf

Ward, K., Lauf, S., Kleinschmit, B., & Endlicher, W. (2016). Heat waves and urban heat islands in Europe: A review of relevant drivers. *Science of the Total Environment*, *569–570*, 527–539. https://doi.org/10.1016/j.scitotenv.2016.06.119

Winkler, P., Lugauer, M., & Reitebuch, O. (2006). Alpine Pumping. *Promet*, *32*(1), 34–42. https://elib.dlr.de/45955/

WMO. (2006). Initial Guidance to Obtain Representative Meteorological Observations at Urban Sites. *World Meteorological Organisation - Instruments and Observing Methods Report*, *81*, 47 ff. https://library.wmo.int/doc_num.php?explnum_id=9286

Žuvela-Aloise, M. (2017). Enhancement of urban heat load through social inequalities on an example of a fictional city King's Landing. *International Journal of Biometeorology*, *61*(3), 527–539. https://doi.org/10.1007/s00484-016-1230-z

# Appendix

**Tab. A1.** List of all air temperature loggers that were in operation in 2018 and 2019. **N°19** indicates the project-internal logger number for the year 2019, **N°18** indicates the project-internal logger number for the year 2018, **Name** is the name of the logger, **LCZ** corresponds to the assigned local climate zone and **Year** the years in which the respective logger was in operation

| N° 19 | N° 18 | Name | LCZ | Year |
|---|---|---|---|---|
| 1 | 31 | VonRoll PH | 2 | 18/19 |
| 2 | 34 | Europaplatz | 2 | 18/19 |
| 3 | X11 | Rathausgasse II: ca. Höhe Taube (Bar) | 1 | 19 |
| 4 | 68 | Uettligen Umland | D | 18/19 |
| 5 | X3 | Sportplatz/Familiengarten vor Egelsee | B | 19 |
| 6 | 35 | Bümpliz Fröschmattstrasse | 6 | 18/19 |
| 7 | 50 | Kreuzung Brunnmatt-Schwarztorstrasse | 2 | 18/19 |

| | | | | |
|---|---|---|---|---|
| 8 | 47 | Wankdorf ESP | 5 | 18/19 |
| 9 | 73 | Bremgartenfriedhof | B | 18/19 |
| 10 | 23 | Länggasse, Neufeldstrasse 135 | 5 | 18/19 |
| 11 | X8 | Viererfeld Veloweg | D | 19 |
| 12 | X5 | Egelsee Süd I: Gantrischstrasse 52 | 5 | 19 |
| 13 | 13 | Egelsee | G | 18/19 |
| 14 | 14 | Helvetiaplatz | 5 | 18/19 |
| 15 | X12 | Waisenhausplatz I (Ostseite): Vor Rest. Grissini | 2 | 19 |
| 16 | 1 | Bubenbergplatz | 2 | 18/19 |
| 17 | 17 | Rosengarten | B | 18/19 |
| 18 | 49 | Aegertenstrasse 53 | 6 | 18/19 |
| 19 | 19 | Galgenfeld Neubausiedlung | 5 | 18/19 |
| 20 | 25 | Umland Köniz | D | 18/19 |
| 21 | 21 | Gaswerkareal Industrie EWB | E | 18/19 |
| 22 | 22 | Matte Mühleplatz | 2 | 18/19 |
| 23 | 70 | Ostermundigen, Ahornstrasse 16 | 6 | 18/19 |
| 25 | 44 | Köniz Neubausiedlung | 5 | 18/19 |
| 26 | 20 | Inselspital | 1 | 18/19 |
| 28 | X7 | Pärkli bei Eigerplatz | 2 | 19 |
| 29 | X1 | Paul Klee, Senke “Familienspaziergang” | D | 19 |
| 30 | 27 | Galgenfeld Industrie | 10 | 18/19 |
| 31 | 63 | Köniz Aussenquartier | 5 | 18/19 |
| 32 | 38 | Bremgartenwald | A | 18/19 |
| 33 | 6 | Dählhölzli-Wald | A | 18/19 |
| 34 | 40 | Kasernenareal | 5 | 18/19 |
| 35 | X6 | Egelsee Süd II: Bürglenstrasse 28 | 6 | 19 |
| 36 | 42 | Viktoriarain | 5 | 18/19 |
| 37 | 37 | Lorraine, Steckweg 15 | 5 | 18/19 |
| 38 | 36 | Spiegel | 6 | 18/19 |
| 39 | 67 | Weyermannshaus Industrie | 8 | 18/19 |
| 40 | X10 | Rathausgasse I: St. Peter & Paul Kirche | 2 | 19 |
| 41 | 41 | Monbijou-Park | B | 18/19 |
| 42 | 10 | Gerechtigkeitsgasse 55 | 2 | 18/19 |
| 45 | 45 | Zytglogge | 2 | 18/19 |
| 46 | 28 | Autobahnausfahrt Wankdorf | E | 18/19 |
| 47 | X14 | Waisenhausplatz III (Mitte): Neben Brunnen | 2 | 19 |
| 48 | 48 | Viererfeld | B | 18/19 |
| 50 | X2 | Kreuzung Familienspaziergang / Laubeggstrasse | D | 19 |
| 51 | 60 | Bümpliz Stöckacker | 4 | 18/19 |
| 52 | 18 | Umland Bümpliz | D | 18/19 |
| 53 | 39 | Breitenrain, Waffenweg | 5 | 18/19 |
| 54 | X15 | Waisenhausplatz IV (Pocketpark): vor Starbucks | 2 | 19 |
| 55 | 55 | Bollwerk (Strasseninsel) | 2 | 18/19 |
| 57 | 65 | Eigerplatz | 2 | 18/19 |
| 58 | 26 | Murifeld (vor Wohnturm 3) | 4 | 18/19 |
| 59 | 33 | Schlossmatte Familiengärten | 9 | 18/19 |
| 60 | 80 | Roschistrasse | 5 | 18/19 |
| 61 | 69 | Westside Center | 8 | 18/19 |
| 62 | 62 | Felsenhaldenweg | 6 | 18/19 |
| 63 | 52 | Wylergut, Jaunweg 11 | 6 | 18/19 |
| 64 | 64 | Bollwerk (Referenz) | 2 | 18/19 |
| 65 | 71 | Umland Bolligen | D | 18/19 |
| 68 | 12 | Gleisfeld Welle | E | 18/19 |
| 69 | 53 | Eisenbahnquartier | 6 | 18/19 |
| 70 | 15 | Bundesplatz | 2 | 18/19 |
| 71 | 9 | Hirschengraben | 2 | 18/19 |
| 73 | 51 | Obstberg, Wattenwylweg 32 | 6 | 18/19 |
| 74 | X13 | Waisenhausplatz II (Westseite): Vor Rest. Luce | 2 | 19 |
| 76 | 76 | Wabern, Viktoriastrasse 9 | 6 | 18/19 |
| 77 | X9 | Viererfeld Wald | A | 19 |

| | | | | |
|---|---|---|---|---|
| 78 | 78 | Dalmazibrücke | G | 18/19 |
| 79 | 79 | Umland Bolligen | D | 18/19 |
| 80 | 32 | Elfenau Krz. Hofmeister-Matterstrasse | 6 | 18/19 |
| 82 | 4 | Thunplatz | 6 | 18/19 |
| 83 | 83 | Stadtlabor | 5 | 18/19 |
| 85 | X4 | Ensingerstrasse 28 | 5 | 19 |
| 86 | 2 | Ostermundigen, Lötschenstrasse 13 | 6 | 18/19 |
| 87 | 87 | Engehalde Stauwehr | G | 18/19 |
| 99 | 99 | Zollikofen Referenz 3m | D | 18/19 |
| 101 | 101 | Steinhölzliwald | A | 18/19 |
| 102 | 86 | Vorderes LG-Quartier, Falkenweg 5 | 6 | 18/19 |
| - | 3 | Thormannstrasse 62 | 6 | 18 |
| - | 8 | Ostring Autobahn | 5 | 18 |
| - | 11 | Bahnhofplatz (Perron C) | 2 | 18 |
| - | 16 | Münsterplattform | 2 | 18 |
| - | 29 | Breitenrain, Wiesenweg | 6 | 18 |
| - | 30 | Weyermannshaus Schwimmbad | B | 18 |
| - | 46 | Breitenrain, Melchtalstrasse | 5 | 18 |
| - | 54 | BEA Expo | 5 | 18 |
| - | 56 | Altstadt Nord | 2 | 18 |
| - | 57 | Tscharnergut | 4 | 18 |
| - | 58 | Wabern | 8 | 18 |
| - | 59 | Kreuzung Kapellen-Belpstrasse | 5 | 18 |
| - | 61 | Gaskessel (Veloweg) | B | 18 |
| - | 74 | Welle 7 | 2 | 18 |
| - | 77 | Gleisfeld Güterbahnhof | E | 18 |
| - | 82 | Kursaal, Schänzlihalde 11 | 5 | 18 |

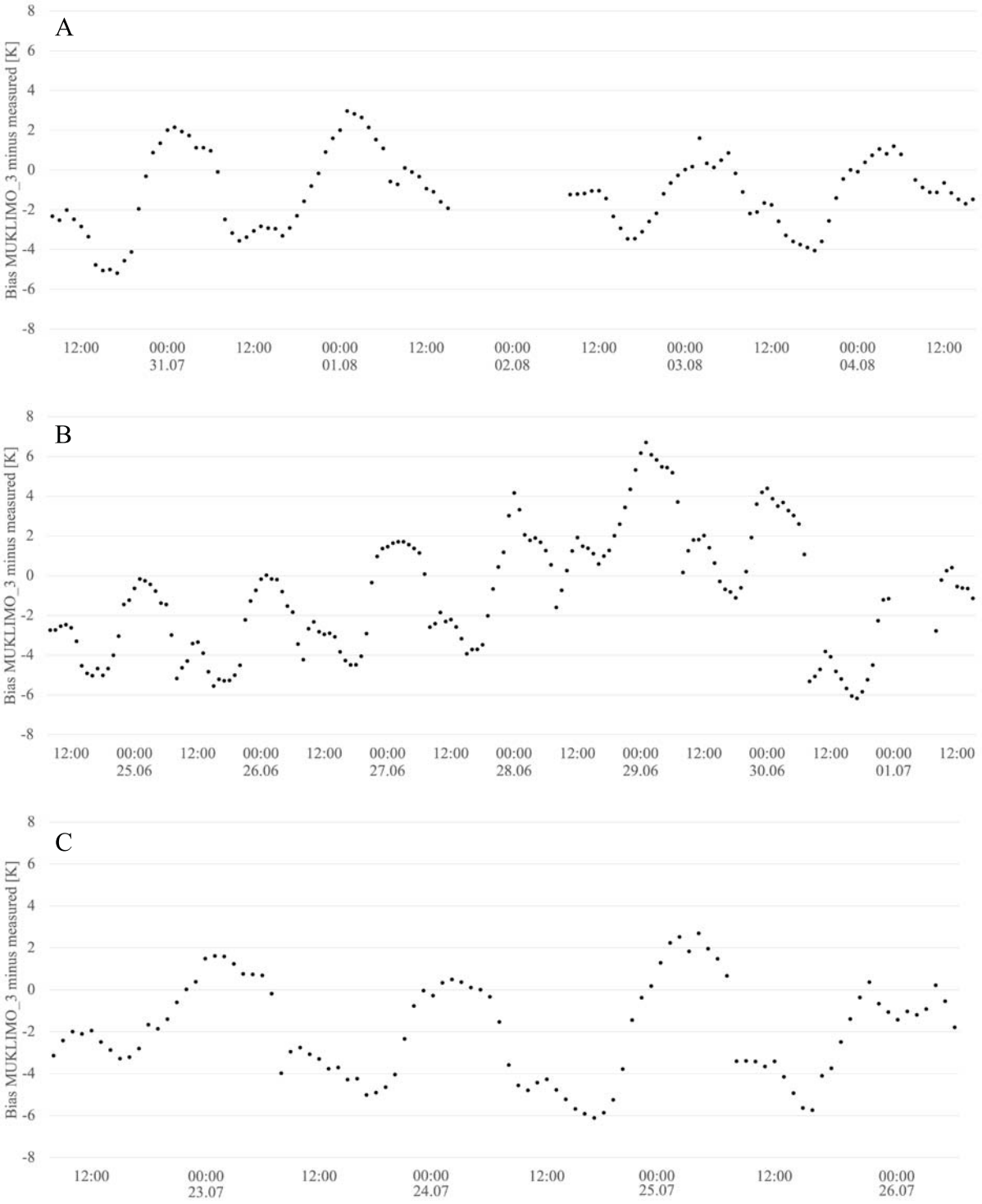


**Fig. A1.** Plots of median hourly air temperature difference of MUKLIMO_3 at 3 m above ground and the measured air temperature for all measurement sites over the entire course of the respective heat wave for **A** HW18, **B** HW19.1, and **C** HW19.2. Gaps in the series correspond to the removed precipitation periods and the subsequent hours of the respective model run.

# Declaration of consent

on the basis of Article 30 of the RSL Phil.-nat. 18

Name/First Name: Hürzeler André

Registration Number: 11-738-572

Study program: Master of Science in Climate Sciences

Bachelor ☐ Master ☑ Dissertation ☐

Title of the thesis: Assessment of the urban climate model MUKLIMO_3 for three heat waves in Bern

Supervisor: Prof. Dr. Stefan Brönnimann

I declare herewith that this thesis is my own work and that I have not used any sources other than those stated. I have indicated the adoption of quotations as well as thoughts taken from other authors as such in the thesis. I am aware that the Senate pursuant to Article 36 paragraph 1 litera r of the University Act of 5 September, 1996 is authorized to revoke the title awarded on the basis of this thesis.
For the purposes of evaluation and verification of compliance with the declaration of originality and the regulations governing plagiarism, I hereby grant the University of Bern the right to process my personal data and to perform the acts of use this requires, in particular, to reproduce the written thesis and to store it permanently in a database, and to use said database, or to make said database available, to enable comparison with future theses submitted by others.

16 August 2021 / Bern

Place/Date

André Hürzeler Digitally signed by André Hürzeler
Date: 2021.08.16 15:55:59 +02'00'

Signature